ZENITH ACADEMIC CROSS-BORDER
ZAC
ILLUMINATING MINDS,
INSPIRING PROGRESS

ISSN 3049-7787 (Print)
ISSN 3049-7795 (Online)

Sustainable
Engineering and Technological Sciences (SETS)

https://sets.zenithacademic.co.uk/index.php/sets/index

Volume 01, Issue 02, 2025

Published by: Zenith Academic cross-border (ZAC)
https://zenithacademic.co.uk/

Blank Page

Sustainable

Engineering and Technological Sciences

https://sets.zenithacademic.co.uk/index.php/sets/index

Sustainable Engineering and Technological Sciences
DOI Prefex: 10.70516/

ISSN 3049-7787 (Print)
ISSN 3049-7795 (Online)

Contents

Sustainable Engineering and Technological Sciences (SETS)

Volume 01, Issue 02 (2025)

Blank Page

Sustainable
Engineering and Technological Sciences
https://sets.zenithacademic.co.uk/index.php/sets/index

Sustainable Engineering and Technological Sciences, 01(01), 2025, pp. 71-81
DOI: https://doi.org/10.70516/8tk3qp78

ISSN 3049-7787 (Print)
ISSN 3049-7795 (Online)

Breakage Time of Bubble in a Stirred Tank for Different Impeller Geometries, An Experimental Investigation

Muayad F. Hamad[1,a*], Basim O. Hasan[1,b], Hasan Sh. Majdi[2,c], Abbas Al-Farraji[1,d]

[1] Department of Chemical Engineering, Al-Nahrain University, Baghdad, Iraq
[2] Department of Chemical Engineering and Petroleum Industries, Al-Mustaqbal University College, Babil, Iraq.

[a] Corresponding author's email: muayad.f.hamad@nahrainuniv.edu.iq (https://orcid.org/0000-0003-4067-159X)
[b] basim.o.hasan@nahrainuniv.edu.iq (https://orcid.org/0000-0001-6774-562X)
[c] hasanshker1@gmail.com (https://orcid.org/0000-0001-7871-9048)
[c] abbas.m.abdulkareem@nahrainuniv.edu.iq (https://orcid.org/0000-0001-5327-8581)

Article info

Received 15 September 2024

Revised 8 December 2024

Accepted 10 December 2024

Available online 1 January 2025

Keywords: *Breakup Time; Impeller Geometry; Stirred Tank; Breakup Probability; Birth Rate.*

Abstract. The successful tank stirring operation requires extensive studies for selecting a suitable impeller design for the dispersion processes in such systems. In this context, the effects of impeller geometry and Reynolds number (Re) on bubble breakage time were investigated to gain a deeper understanding of the breakage phenomena. Three different impeller geometries were investigated: a 4-Twisted blades impeller (4TB), a 4-Flat blades impeller (4FB), and a 2-Flat blades impeller (2FB) For Re range of 18380 to 40830 (based on impeller diameter). Three different time intervals were recognized during the mother bubble's motion; initial breakage time, final breakage time, and retention time. The initial and final breakage times were calculated by following the injected bubble using a high speed camera at different zones around and in the impeller region. It was found that the breakage time decreases with increasing Reynolds number (or stirring speed) for all geometries. The 4-Flat blades impeller showed the lowest breakage time indicating the highest breakage rate. For 4-FB impeller, it decreases by about 20% when the Re increases from 18380 to 40830. The breaking interval increases with increasing Re and is lowest for 4FB impeller. The increase is for 4FB is 65%.

1. Introduction

Dispersion phenomena is a case widely encountered in industrial applications such as bioreactors, two phase mixing, separation processes in petroleum industry, extractions, etc. The characterization of breakage behavior of fluid particles (bubbles/drops) in agitated tanks has a scientific significance from the operational and design stand points with further investigations still required [1,2].

The time taken by the motion of the bubble in a turbulent field plays an important role in affecting the breakup rate, and consequently it affects the rates of mass and heat transfer. The length of time a bubble stays in the impeller zone can result in more fragmentation of bubble due to the longer exposure to high turbulence levels and shearing effects. The bubble retention close to the impeller, has been observed and discussed by some previous works [3–5]. It has been found that the retention interval is influenced by the hydrodynamics in the impeller vicinity. Studies reporting the experimental determination of residence time and its effect on the fluid particle breakup is currently limited in literature. The structures of flow current in the impeller region have been studied by several authors[e.g. 6–8]. Those studies indicated the complexity of the hydrodynamics around the impeller which results in an unpredictable dynamic behavior of fluid particles.

The stirred tanks breaks the gas bubbles (or drops) into smaller bubbles. This entrainment increase the residence time and interfacial aera between the gas and liquid, thereby allowing more mass (or heat) transfer into the process [9]. The breakage location is directly related to the time spent by the bubble in the impeller region. The time interval of each bubble staying in the impeller region causes the bubbles to spend more time exposed the turbulent eddies and shear forces provided by the impeller [1,10]. This can increase the BP and number of fragments. This time was observed to be dependent on the stirring speed (or Re), initial bubble size, and impeller geometry [5,11,12] .

The breakage time in this investigation is considered to be the time between the beginings of the bubble's deformation to the instant that the bubble has produced the final number of fragments, e.g. the final breakage has occurred [4,13,14]. Several authors [15–19] proposed that the breakage time is the time taken from initial deformation to the instant of the occurrence of first breakage which is called the initial breakage time.

The results obtained from single bubble breakage experiments are proved to be successful in understanding the behavior of bubbles of a particular size distribution [9]. Experimental determination of breakage time of a bubble in the impeller region using high speed imaging helps to better understanding the breakage dynamics occurring in stirred tanks.

The impeller design has an important influence on the breakage rate as it affects the intensity of turbulence and energy dissipation rate in the impeller region leading to affect the local breakages [20–22]. The breakage behavior of the bubble is affected by the design of the impeller as this design feature determines the flow patterns within the tank [23]. The impeller geometry also affects the shear stress exerted on the fluid particle and the energy dissipation rate, and thus, it affects the breakage rate depending on the operational parameters such as stirring speed and the fluid's physical properties. In addition, the impeller geometry influences the bubble's trajectory in the tank, the probability of collision with the blade(s) and the breakage rate [11,24]. The impeller geometry also affects the length of time the bubble remains close to the impeller by influencing the strength of the turbulent eddies and flow currents that may retain the mother bubble. in the high turbulence level region producing more daughter bubbles.

This current work follows on from Alabdaly et al [11] who studied and presented the effects of impeller geometry on the breakage rate for different stirring speeds (Re). This current work presents an investigation to determine the breakage time of the single bubble for the same impeller geometries and stirring speeds presented earlier under different operating conditions.

The breakage time in this investigation is considered to be the time between the beginings of the bubble's deformation to the instant that the bubble has produced the final number of fragments, e.g. the final breakage has occurred [4,13,14].

2. Experimental setup

Figure 1 shows a sketch of the apparatus. The experimental rig has been described in detail in Alabdaly et al, [11]. Briefly, the rig comprised a cylindrical tank made from Perspex, which is filled with the continuous phase (water). The cylindrical tank is surrounded by an outer rectangular Perspex tank, again filled with water to avoid the light reflections and distortion that can affect the quality image produced. The other equipment used during the experiments include a high-speed camera (Phantom, Miro C110), a mechanical stirrer, an impeller (three geometries), an air compressor for injecting the mother bubble, a LED illumination, control valve for controlling the injection rate of mother bubbles, and a Teflon tube for air injection to the tank. The frame rate of the high-speed camera was set to 1000 fps, which was founf enough to capture the bubble breakage around the impeller at a resolution of 1280 × 800. Three different impeller geometries were used, 4-Twisted blades impeller, 2-Flate blades impeller, and a 4-Flate blades impeller (details of the dimensions of each impeller and photos are presented in Alabdaly et al [11].

Three values of agitation speed were investigated; 180 rpm, 290 rpm, and 400 rpm. The corresponding values of Reynolds numbers (Re) are 18380, 26900, and 40830 which are calculated using [25,26]:

$$\mathrm{Re_i} = \frac{\rho N D_i^2}{\mu} \tag{1}$$

where, Di is the impeller's diameter, ρ is the density of the continuous phase, μ is the viscosity of continuous phase, and N is the stirring speed (rev/s).

The experimental procedure has been described in detail in the previous work [11]. Briefly, the mother bubble is released below the impeller by a distance of 70 mm. The injection location is 50 mm away from the tank's wall. The mother bubble is injected at a position below the impeller ensuring that the released bubble passes through the impeller region. The mother bubbles were injected at a rate of 1 bubble per 4 seconds. A glass tube was used to surround the injection tube to guarantee the released bubble was the same size for all Re. The average diameter of the mother bubbles for all Re, was measured to be 4.5 mm ±0.2 mm.

The motion of the injected bubble was recorded using a high-speed camera. The recording was then used to obtain the initial breakage time and final breakage time for each geometry and Re. For each condition investigated, at least 500 injection tests were conducted. This was sufficient for obtaining results of statistical significance. The breakage probability (BP) was via [27]:

$$\mathrm{BP}\ \% = \frac{\mathrm{n}}{\mathrm{n_T}} \times 100 \qquad (2)$$

The used high speed camera provides fast recording ability to record the events during the fast motion in impeller zone. These videos, using the software provided for this camera, can be played very slowly to analyze the motion and the breakage behavior. Besides, this camera provides a time record to a digit 10-9 from the second. From this time record, accurate time measurements can be obtained. Table 1 presents the uncertainty of experimental parameters.

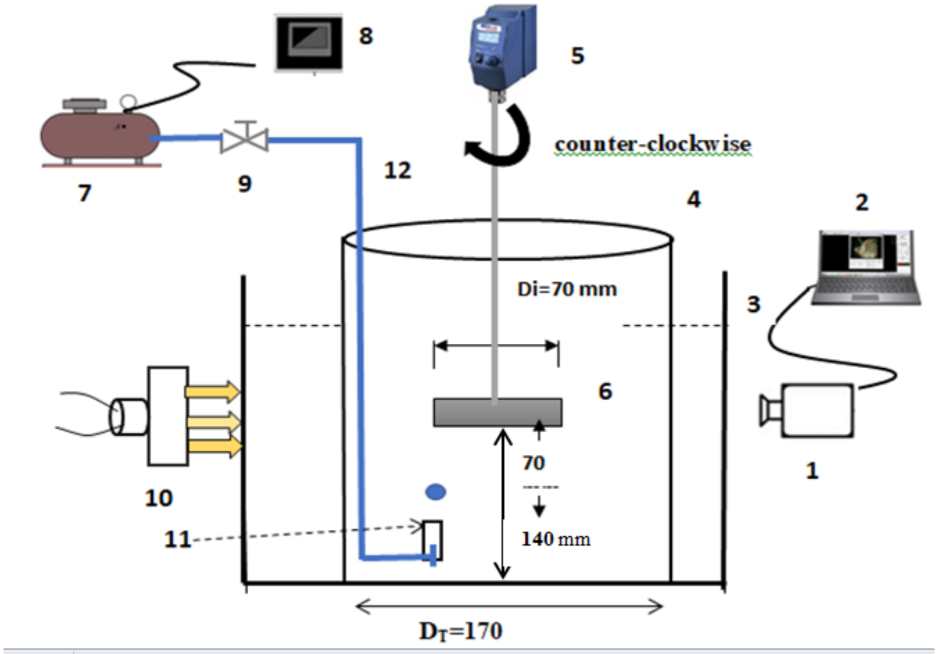

Figure 1: Experimental Fig, (1)phantom camera (high speed) (2) personal computer, (3) perspex tank, (4) internal perspex tank, (5) agitator, (6) perspex impeller, (7) regulator, (8) compressor, (9) control valve, (10) light projector, (11) framing tube, (12) Teflon tube [11].

Table 1: Experimental variables and results uncertainty.

Parameter	Deviation%
Re	±1.6%
Breakage time, ms	±15.5%
breakage probability	± 11.1%
Room temperature, ºC	± 1.0 ºC

3. Results and Discussion

3.1 The Breakage probability (BP)

Figure 2a shows the trends of BP with Re for the three impeller geometries investigated based on the results of the authors' previous work [11]. It can be seen that, for the three impeller types, there is a noticebale increase of PB with Re. The 4FB impeller gives highest value of BP, while 4TB impeller gives the lowest. The high breakage probability of 4- Flat blades impeller (4FB) is attributed to the high collision rate of bubbles with the blades and due to strength of turbulent fluctuations provided by this geometry and high shearing effect[11].

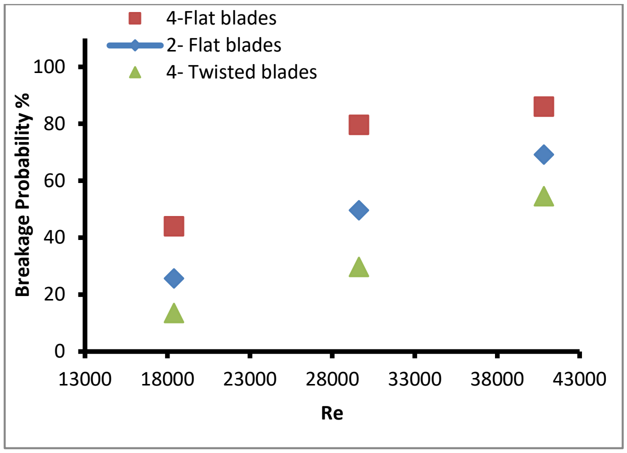

Figure 2a. BP vs. Re for different impeller geometries [11].

3.2 Breakage time

The breakage time (t_b), in this work, is adopted to be the time between the moment when the the bubble deforms by 10% and the moment of the occurrence of first breakage [10]. The interval between the oocurence of first breakage and last breakage, which includes generation of more daughter bubbles, is considered the breakaing interval (t_f). During this interval the bubble undergoes further breakages that produce the final population of fragments (daughter bubbles). The videos show that at a relatively high Re, the bubbles are retained close to blades for an more time. The “retention time” (t_r) of the bubble close to the blades, where the energy dissipation rate is high, is noticed to be an important factor that allows continuous breakup due to the longer exposure of the daughter bubble to the influence of high energy turbulent eddies. This region has been reported to be at a distance of about two blades height from the impeller blade [6]. Figure 2b presents a sketch showing the breakage intervals during the bubble’s motion from the release point until leaving the “impeller region”.

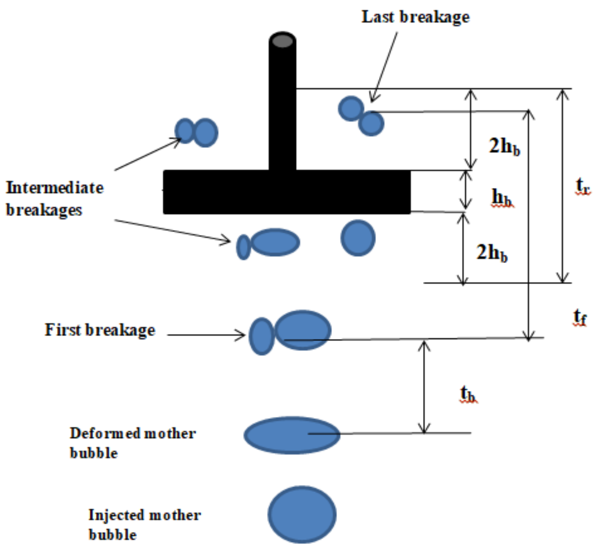

Figure 2b: Different time intervals for bubble breakage events, t_b is the breakage, t_f the breaking interval, and t_r is the retention time.

Figures 3a through 3c presents some typical images showing bubble breakage times for different Re for the 2FB impeller. It is evident from Figure 3a that the breakage time is 153.3 ms at Re=29600 for 2FB impeller. While Figure 3b for Re=40830 the time taken until the occurrence of first breakage is 87.7 ms and that of last breakage is 154.4 ms. Figure 3c, shows the breakage time for the 4TB impeller is 174 ms. It was observed that the 4-Twisted blade impeller gives longer breakage time than the other geometries.

Figure 4 presents the average breakage time (taken for at least 100 breakage events) versus Re for the different impeller geometries. It is clear that when Re increases, the the breakage time decreases for the three geometries. This is in agreement with the reported results of Kenno et al [28] and Hasan and Krakau [10]. In addition, the 4FB impeller gives the lowest average breakage time and the 4TB impeller gives the highest average breakage time. The decrease in breakage time with increasing Re is ascribed to the increase in turbulence strength and therefore increased rates of bubble collision with the turbulent flow structures.

The low values of breakage time for 4FB impeller is ascribed to the high shearing effect and turbulence level provided by this geometry of four flat blades [11]. The high increased interaction between bubbles and blades, including bubble –blade collision, plays an important role in reducing the time taken between the bubble’s deformation stage and the occurrence of first breakage, i.e. the breakage time.

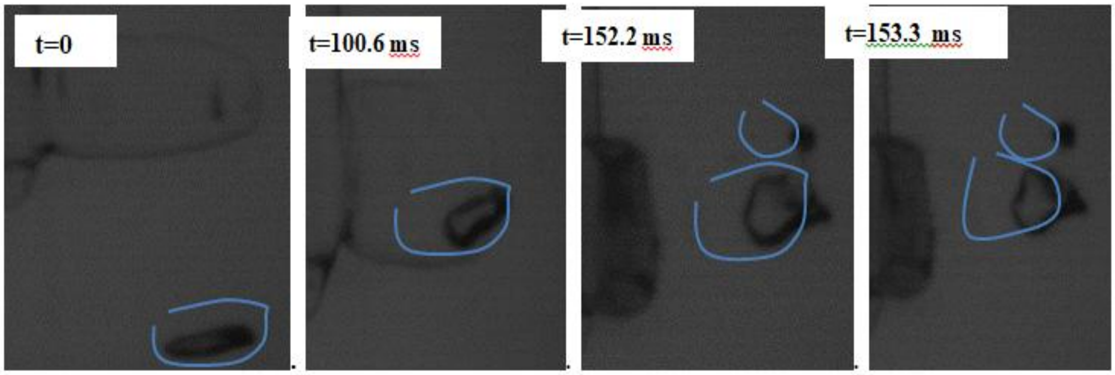

Figure 3a: Breakage time for Re=29600, 2FB impeller.

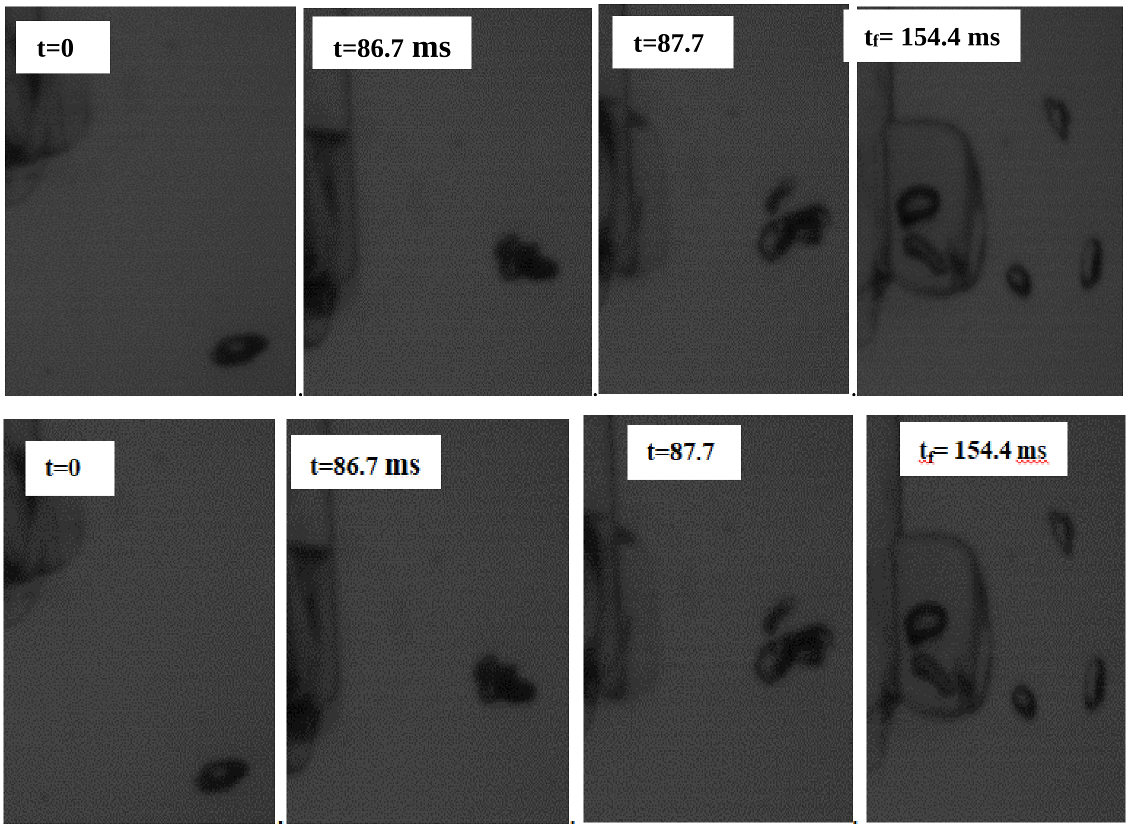

Figure 3b: Breakage time for Re=40830, 2FB impeller.

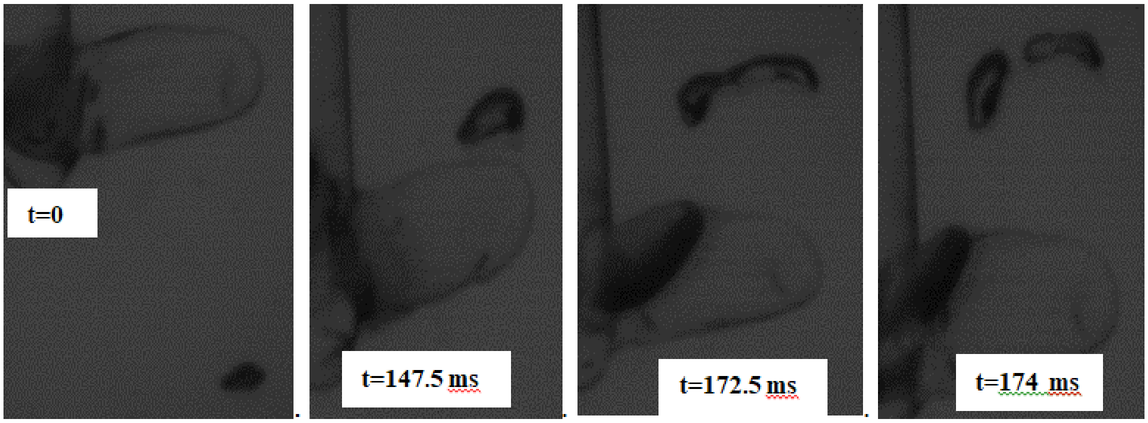

Figure 3c: Breakage time for Re=40830, 4FB impeller.

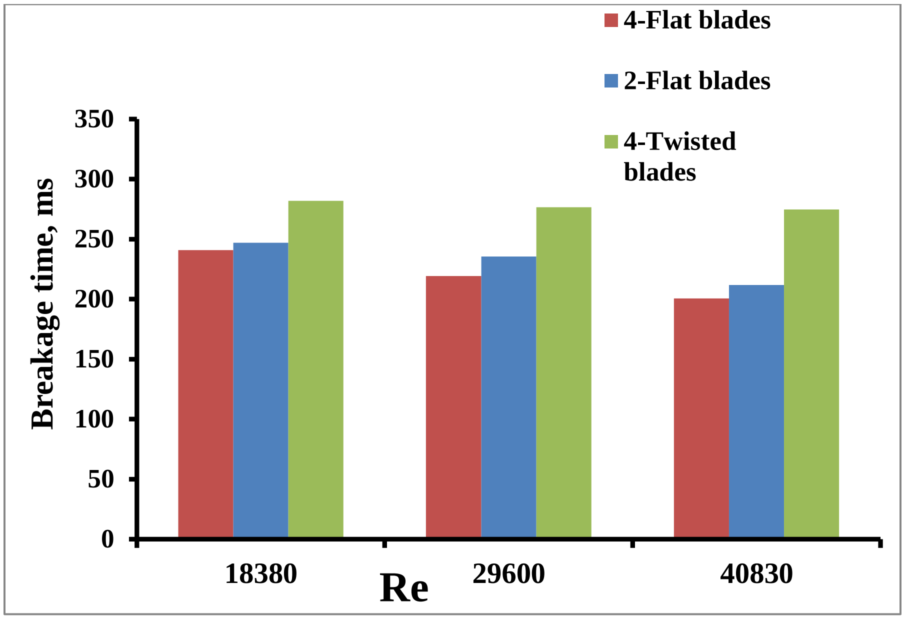

Figure 4: Breakage time vs. Re for three geometries.

3.3 Breaking time interval

The breaking interval, which is time duration taken between the first and last breakages, is function of Re [4]. This time interval includes the generation of more "daughter bubbles" due to the further breakups of the large fragments. The fragmentation persists until the daughter drops are no longer able to break up further due to their small size. Then, the daughter bubbles leave the impeller region due to bouncy forces.

In the current work, the results showed that the duration of this breaking interval is influenced by impeller geometry too. Images in Figures 5 through 7 present some photos as examples for the time taken by the bubble motion from first to last breakage in the impeller region. In these figures the time zero (t=0) is considered to be the time of first breakage. During this time interval more daughter bubbles are produced depending on Re and on the impeller type.

The series of images in Figure 5a show that the time between first and last breakage is 27.5 ms in which 6 daughter bubbles are produced for the 2FB impeller at Re=40830. Figure 5b for the same conditions, 4 daughter bubbles are produced in 107.5 ms. So, this time interval is a subject of large variance because of the complicated hydrodynamics in the impeller zone which may drive the bubble into a region of either high or low energy level resulting in a short or long interval respectively.

Figure 6a presents a some selected of images for bubble breakage around the 4FB impeller with a breaking interval of 62.5 ms during which 9 fragments are produced (one fragment went behind the blades). Figure 6b shows that 7 fragments are produced in breaking interval of 77.5 ms. Figures 7a shows that for 4-Twisted blade 3 fragments are produced in 27.5 ms and Figure 7b shows that 5 fragments are produced in 42.5 ms.

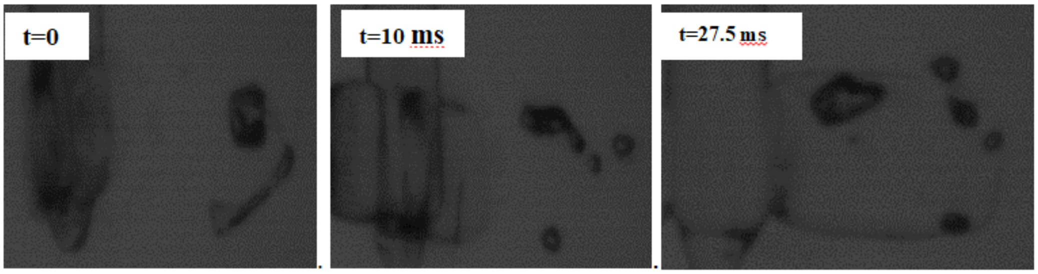

Figure 5a. Fragmentation into 6 daughter bubbles of 2-Flat blades impeller in 27.5 ms, Re=40830.

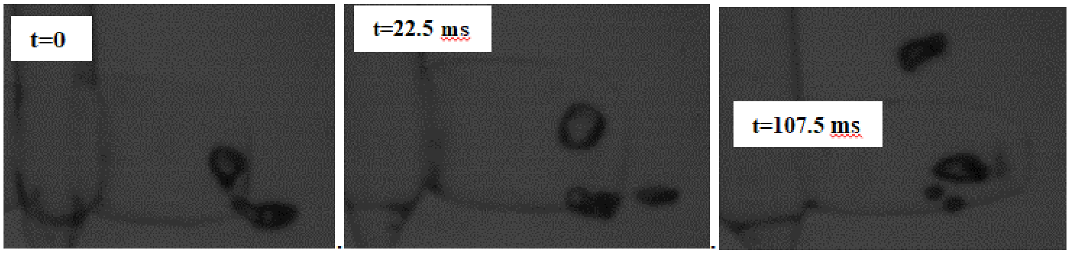

Figure 5b. Fragmentation into 4 daughter bubbles of 2-Flat blades impeller in 107.5 ms, Re=40830.

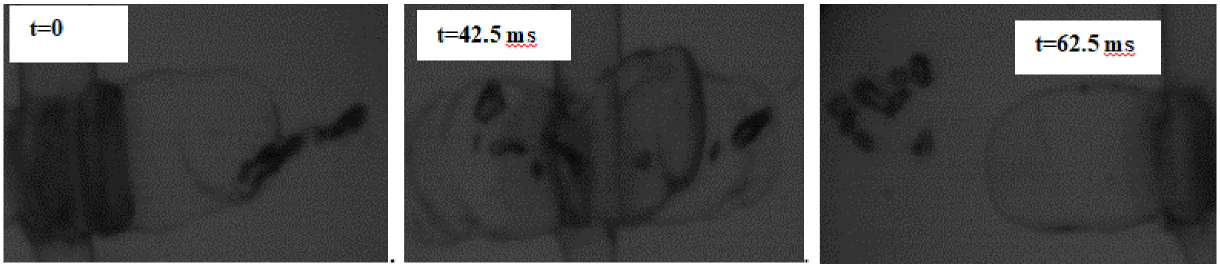

Figure 6a. Fragmentation into 9 daughter bubbles of 4-Flat blades impeller in 62.5 ms, Re=40830.

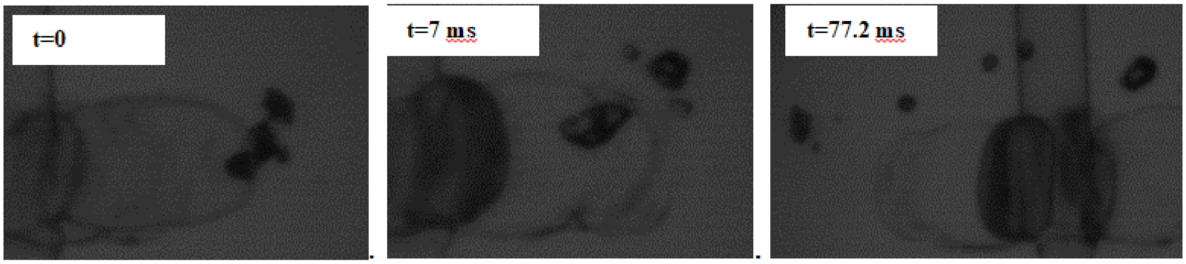

Figure 6b. Fragmentation into 7 daughter bubbles of 4-Flat blades impeller in 77.2 ms, Re=40830.

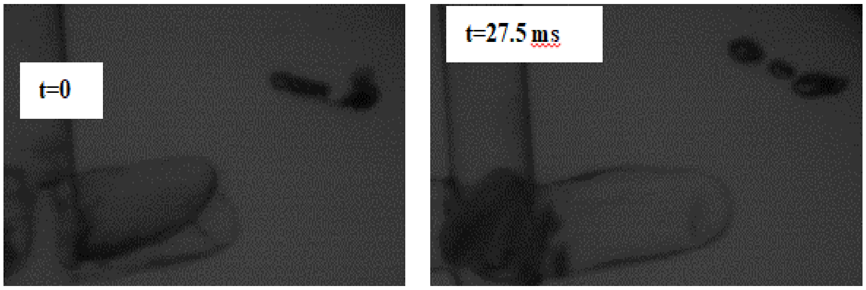

Figure 7a. Fragmentation into 3 daughter bubbles of 4-Twisted blades impeller in 42.5 ms, Re=40830.

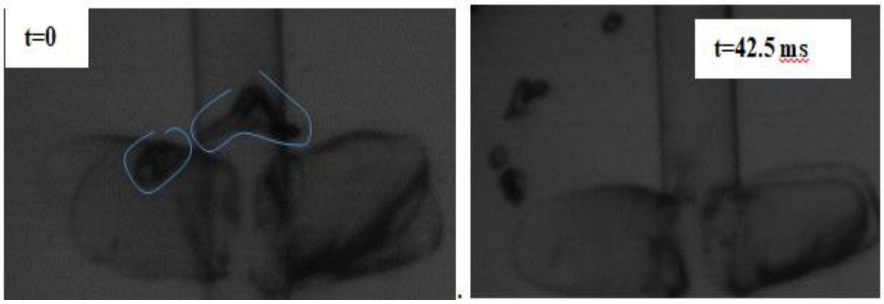

Figure 7b. Fragmentation into 5 daughter bubbles of 4-Twisted blades impeller in 42.5 ms, Re=40830

Figure 8 presents the average value of "breaking interval" aginst Re for the three geometries. It is evident that this interval increases with Re for the three geometries. For 2FB it increases by about 78% when Re increases from 18380 to 40830. This increase is because at higher Re, the bubble is caught by the rotating flow currents around the impeller resulting in a prolonged time exposed to turbulent eddies and shear forces [1,5]. Therefore, more daughter bubbles are produced during this time interval. Figure 8 also reveals that the breaking interval is highest for the 2FB impeller, followed by the 4FB impeller, and then the 4TB blades impeller. The high breaking interval for the 2FB blades and 4FB blades impeller is because these geometries cause complicated hydrodynamics in theimpeller region which retain the bubble for a prolonged time resulting in further fragmentation. The low breaking interval for the 4TB blade geometry is ascribed to the fact that the daughter bubbles leave the impeller region quickly compared to the other geometries. In other words, the retention time for this geometry is low as the flow patterns around the impeller do not hold the bubbles for prolonged time. Table 3 lists the values of retention time of the different geometries measured by high speed camera. This time is considered to start from the first breakage events until the departure of last daughter bubble from the impeller region.

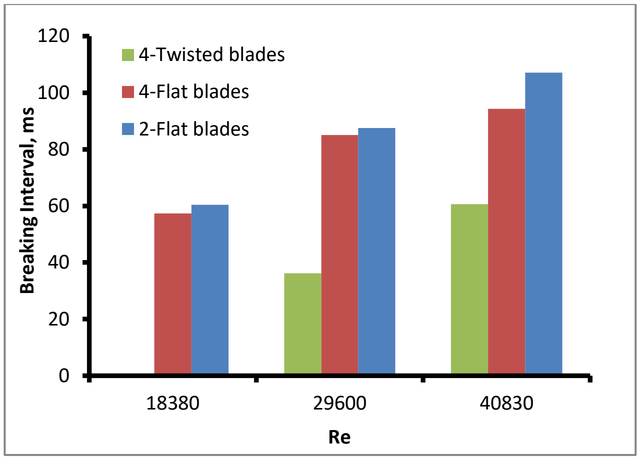

Figure 8: Breaking interval for different impeller geometries.

"Retention time" is an important factor that was observed to be affecting the bubble breakage rate which is found to vary with the impeller geometry and Re. It affects the breakage rate by allowing the daughter bubbles to be exposed to the impeller impact for a prolonged time. This permits the birth of more daughter bubbles especially from large size initially formed daughter bubbles. Table 4 lists the values of retention times for the average of at least 70 breakage events for each condition except for 4TB blades at lowest Reynolds numbe (Re), where the multiple breakages are few and thus, not statistically significant.

In general, the retention of a bubble for a certain time interval in the impeller zone for the case of the 4FB , results in a large number of daughter bubbles compared to 2FB and 4TB due to the longer exposure to the effect of high energy turbulent eddies.

It is evident from Table 2 that the retention time is influenced by the impeller geometry and it increases clearly with increasing Re for all geometries. The increase with Re is due to the increased turbulent motion of flow currents and the formation vortices that catch the bubbles in the vicinity of the impeller. In general, this delay in bubble motion in the high energy region causes the production of further daughter bubbles before all bubbles leave the impeller region. But, the further fragmentation of daughter bubbles during this time interval is also dependent on the strength of flow field and the size of the initially formed daughter bubbles; that will behave as mother bubbles for the subsequent breakages. The hydrodynamical effects around the impeller appear to causes the bubbles to approach the blade's tip which increases the probability of further breakage.

Table 2. Retention time for the used impellers at various Re.

Geometry	**Retention time, ms**		
	Re=18380	**Re=29600**	**Re=40830**
2FB	68.4	96.5	117.1
4FB	64.4	93.0	103.3
4TB	-	40.2	66.6

3.4 Birth rate of daughter bubbles

The average number of "daughter bubbles" produced during the breaking time interval for each geometry is presented in Table 3. It can be seen that the highest number of daughter bubbles is produced by the 4- Flat blade impeller, followed by the 2FBand then the 4TB. Dividing the number of fragments by the breaking time interval gives the average birth rate of the daughter bubbles, which are presented in Figure 9. It can be seen that the highest birth rate of daughter bubbles is for the 4FB impeller while the lowest is for the 4-Twisted blades impeller. This indicates that the 4FB impeller has the most efficient geometry in causing bubble breakage and fragmentation.

Table 3. Number of fragments (average) different geometries

Re	2FB	4FB	4TB
18380	2.4	2.66	2.19
29600	6.57	6.80	2.44
40830	8.79	10.1	4.30

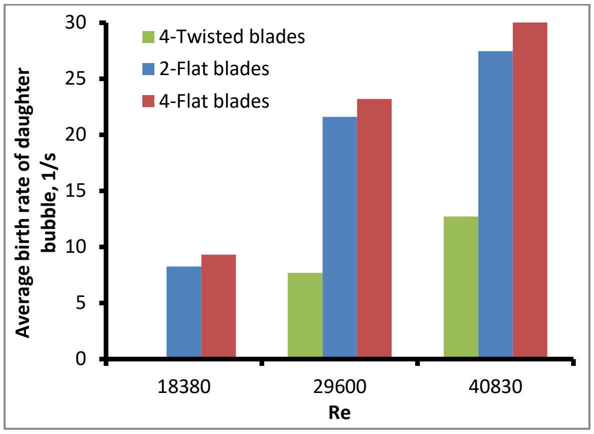

Figure 9. Birth rate of daughter bubbles vs. Re for different geometries.

The high birth rate for the 4FB impeller is attributed to the increase of probability of bubble's shearing off and then colliding with the blade(s). With the relatively long retention time caused by the 4FB impeller, the number of generated fragments increases compared to the other impeller geometries. It is to be noted that the 4FB gives the lowest bubble retention time. This is because the structure of flow field around this impeller does not retain the bubbles for long time and therefore fewer daughter bubbles fragments are made.

4. Conclusions

When a bubble travels in a turbulent field in a stirred tank, it's breakage experiences three time intervals. The first interval is between the initial deformation until the occurrence of first breakage event, which is considered to be the "initial breakage time". The second time interval is between the "first breakage" until the very last breakage which is considered to be the "breaking interval". There is a third time interval in which the bubble is caught and retained by flow currents around the impeller, which is considered to be the "retention time". This retention time starts when the bubble enters the impeller region until the departure of last daughter bubble from this region, which is below and above the impeller by twice the blade height. All of the three time intervals are a function of both Reynolds number and impeller geometry. For all impeller geometries, the breakage time decreases with increasing Re due to the increased interaction between the bubbles and the turbulent eddies in the flow field. The breaking interval and retention time increase with increasing Re because the flow currents around the impeller retain the bubble for a prolonged time close to the impeller. The 4FB impeller provides lower breakage time than 2FB and 4TB blades impellers due to the high energy dissipation rate produced by this impeller. The highest decrease is for 4FB impeller which is 20%, indicating the effcetivness of this geometry. The 2FB impeller produces a longer breaking interval due to the longer retention time in the near impeller region. For this impeller the breaking interval increases by 65% when Re increases to 40830. The 4FB blades impeller produces the highest birth rate of daughter bubbles (34 fragments at highest Re), therefore, it is the most efficient impeller geometry investigated in current work. 4TB impeller, is lowest birth rate of daughter bubbles indicating the low mixing effecincy.

Acknowledgment

The support from "Alexander von Humboldt Foundation/ Germany" to this work is appreciated

Symbols

μ	viscosity, kg/m s
D_i	Impeller diameter, m
N	rotational speed, rpm
Re	Reynolds number
T	time, s
ρ	density, kg/m^3

Abbreviations

2FB	two flate blades
4FB	four flate blades
4TB	four twisted blades
BP	Breakage probability

References

1. B.O. Hasan, M. F. Hamad, H. Sh. Majdi, M. M. Hathal, Experimental characterization of dynamic behavior of single bubble breakage in an agitated tank, European Journal of Mechanics / B Fluids .85 (2021) 430–443. https://doi.org/10.1016/j.euromechflu.2020.11.001
2. H. Zhou, X. Yu, B. Wang, S. Jing, W. Lan, S. Li, Experimental study on drop breakup time and breakup rate with drop swarms in a stirred tank,

AIChE J. 27(2021) 1–21. https://doi.org/10.1002/aic.17065

3. R. Andersson, B. Andersson, Modeling the breakup of fluid particles in turbulent flows ,AIChE, J. 52(2006) 2031–2038. https://doi.org/10.1002/aic.10832
4. B.O. Hasan, Experimental study on the bubble breakage in a stirred tank Part 1: Mechanism and effect of operating parameters, International Journal of Multiphase Flow 97(2017a) 94–108. https://doi.org/10.1016/j.ijmultiphaseflow.2017.08.006
5. B.O. Hasan, Experimental study on the bubble breakage in a stirred tank, Part 2: local dependence of breakage events, Exp. Therm. Fluid Sci. 96 (2018)48–62. https://doi.org/10.1016/j.expthermflusci.2018.02.013
6. H. Hartmanna, J. J. Derksen, C. Montavonb, J. Pearsonb, I. S. Hamillb, van den Akker H E A. Assessment of large eddy and RANS stirred tank simulations by means of LDA, Chem. Eng. Sci. 59 (2004)2419–2432. https://doi.org/10.1016/j.ces.2004.01.065
7. A. Zamiri, J. T. Chung, Numerical evaluation of turbulent flow structures in a stirred tank with a Rushton turbine based on scale-adaptive simulation Computers & Fluids 170(2018)236–248. https://doi.org/10.1016/j.compfluid.2018.05.007
8. J. Ramírez-Cruz, M. Salinas-Vázquez, G. Ascanio, W. Vicente-Rodríguez, C. Lagarza-Córtes, Mixing dynamics in an uncovered unbaffled stirred tank using Large- Eddy Simulations and a passive scalar transport equation, Chemical Engineering Science, 222(2020)115658. https://doi.org/10.1016/j.ces.2020.115658
9. M. S. N. Oliveira, A. W. Fitch, X. NI. A study of bubble velocity and bubble residence time in a gassed oscillatory baffled column, Effect of Oscillation Frequency, Trans IChemE, Vol. 81, Part A, (2003) 233-242. https://doi.org/10.1205/026387603762878692
10. B.O. Hasan, F. Krakau, Experimental study on the bubble breakage in a stirred tank. Part 1. Mechanism and effect of operating parameters Int. J. Multiph. Flow 97(2017) 94–108. https://doi.org/10.1016/j.ijmultiphaseflow.2017.08.006
11. H.A. Alabdly , H. Sh. Majdi, M. F. Hamad, M. M. Hathal, B.O. Hasan, Effect of impeller geometry on bubble breakage and the contributions of different breakage mechanisms in a stirred tank, Fluid Dyn. Res., 52(2020) 1–24. https://doi.org/10.1088/1873-7005/abbe97
12. E. Herø, H. Forgia, J. Solsvik, H. A. Jakobsen, Single drop breakage in turbulent flow: Statistical data analysis, Chemical Engineering Science: X8(2020) 100082. https://doi.org/10.1016/j.cesx.2020.100082
13. Maluta, F., Hydrodynamics, power consumption and bubble size distribution in gas-liquid stirred tanks, Chemical Engineering Research and Design, 194 (2023) 582–596. https://doi.org/10.1016/j.cherd.2023.05.006
14. J. Solsvik, H. Jakobsen, Single drop break up experiments in stirred liquid–liquid tank, Chem. Eng. Sci. 131 (2015a) 219–234. https://doi.org/10.1016/j.ces.2015.03.059
15. V. Hancil, V. Rod, Break-up of a drop in a stirred tank, Chem. Eng. Process. 23(1998) 189–193. https://doi.org/10.1016/0255-2701(88)80015-1
16. S. Maass, A. Gabler, A. Zaccone, A. Paschedag, M. Kraume, Experimental investigations and modeling of breakage phenomena in stirred liquid/liquid systems, Chem. Eng. Res. Des. Trans. IChemE A 85 (A5) (2007) 703–709. https://doi.org/10.1205/cherd06187
17. M. Stork, Model-based Optimization of the Procedure of Emulsification, PhD thesis, Technical University Delft, Netherlands, 2005.
18. S. Maass, M. Kraume, Determination of breakage rates using single drop experiments, Chem. Eng. Sci. 70 (2012) 146–164. https://doi.org/10.1016/j.ces.2011.08.027
19. Y. Shuai, X.Wang, Z. Huang, J. Sun, Y. Yang, Experimental measurement of bubble breakup in a jet bubbling reactor, AIChE Journal, 67(2021) 1. https://doi.org/10.1002/aic.17062
20. M. Martin, F. Montes J, M. Gal'an, Bubbling process in stirred tank reactors I: agitator effect on bubble size, formation and rising Chem. Eng. Sci.

63 (2008a) 3212–3222. https://doi.org/10.1016/j.ces.2008.03.028

21. B. Prakash, T. S. Milinkumar, V. K. Pareek, R. P. Utikar, Impact of HSPBT blade angle on gas phase hydrodynamics in a gas–liquid stirred tank, Chemical Engineering Research and Design 130 (2018)219–229. https://doi.org/10.1016/j.cherd.2017.12.028
22. D. Mesa, R. Pablo, Brito-Parada, Bubble size distribution in aerated stirred tanks: Quantifying the effect of impeller-stator design, Chemical Engineering Research and Design 160(2020) 356–369. https://doi.org/10.1016/j.cherd.2020.05.029
23. M. Martin, F. Montes, M. Galan, Influence of impeller type on the bubble breakup process in stirred tanks, Ind. Eng. Chem. Res. 47(2008b) 6251–6263. https://doi.org/10.1021/ie800063v
24. C. Bliatsiou, A. Malik, L. Böhm, M. Kraume, Influence of Impeller Geometry on Hydromechanical Stress in Stirred Liquid/Liquid Dispersions, Ind. Eng. Chem. Res., 58(2019) 2537−2550. https://doi.org/10.1021/acs.iecr.8b03654
25. S. M. Harriott (). Unit Operations of Chemical Engineering 6th ed., McGraw-Hill International, New York, 2001.
26. B.O. Hasan, M.A Sahir.. Corrosion of carbon steel in two phase flow (CO2 gas-CaCO3 solution) controlled by sacrificial anode, Journal of Natural Gas Science and Engineering, 46(2017) 71-79. https://doi.org/10.1016/j.jngse.2017.06.032
27. C.A. Coulaloglou, L.L. Tavlarides, Description of interaction processes in agitated liquid–liquid dispersions. Chem. Eng. Sci. 32 (11) (1977) 1289–1297. https://doi.org/10.1016/0009-2509(77)85023-9
28. M. Konno, A. Aoki, S. Saito, Scale effect on breakup process in liquid-liquid agitated tanks. J. Chem. Eng. Jpn. 16 (4) (1983) 312–319. https://doi.org/10.1252/jcej.16.312

Blank Page

Sustainable
Engineering and Technological Sciences
https://sets.zenithacademic.co.uk/index.php/sets/index

Sustainable Engineering and Technological Sciences, 01(02), 2025, pp. 12-31
DOI: https://doi.org/10.70516/j215nh63

ISSN 3049-7787 (Print)
ISSN 3049-7795 (Online)

An Airfoil Science Including Causality

Adam Suppes [1,a], Galen Suppes[2,b*], Arnold A. Lubguban[3,c] , Harith H. Al-Moameri[4,d]

[1] Suppes Engineering Technologies, 5400 S Hyde Park Blvd Apt D7, Chicago, IL 60615-5852.
[2] HS-Drone LLC, 710 Lexington Ave., Charlottesville, VA 22902.
[3] Center for Sustainable Polymers, Mindanao State University-Iligan Institute of Technology, Iligan City 9200, Philippines
[4] Materials Engineering Department, Faculty of Engineering, Mustansiriyah University, Baghdad 35010, Iraq.

[a] asuppes@seas.upenn.edu (https://orcid.org/0009-0007-5719-7907)
[b] Corresponding author's email: suppesg@hs-drone.com (https://orcid.org/0000-0002-3076-4955)
[c] arnold.lubguban@g.msuiit.edu.ph. (https://orcid.org/0000-0001-6077-8234)
[d] almoamerih@uomustansiriyah.edu.iq; almoamerih@ alnaji-uni.edu.iq. (https://orcid.org/0000-0001-5985-0235)

Article info
Received 11 January 2025
Revised 29 April 2025
Accepted 05 May 2025
Available online 1 July 2025

Keywords: *Airfoil; Air Flow; Aerodynamic; Lift Forces; Simulation; Computational Fluid Dynamic.*

Abstract. Traditional simple explanations of how air flow generates aerodynamic lift neither identify fundamental mechanisms for the generation of lift pressures (i.e. causality) nor account for the many forms of dissipation losses across streamlines. By comparison, the Navier-Stokes equation explicitly includes pressure dissipation and implicitly includes the mechanism for the generation of lift forces in surface boundary conditions. This paper critically evaluates computational fluid dynamic (CFD) simulation results to better understand how lift pressure generation and dissipation impact lift and drag on airfoils and lifting bodies. Three basic-physics' principles emerge as fundamentally correct and insightful on how air flow causes pressures on an airfoil, i.e. "causality," without the complexities of partial differential equations. Examples are provided on how the insight gained from fundamentally-correct simple explanations are advancing new frontiers in solar and ground-effect aviation. Initial steps are taken toward advancement of aircraft design systems-level analysis with lost work analysis and comparisons to ideal performance. 2D CFD simulations of airfoils provide insight into continuum mechanics; examples include multiple airfoils and the Venturi meter. 3D CFD on a thin cambered wing and molecular mechanics approaches are presented which validate the continuum mechanics

1. Introduction

Three basic principles of physics identify how air flow causes aerodynamic lift, specifically:

Principle 1. Impacting air flows create higher surface pressures.

Principle 2. Diverging air flows create lower surface pressures.

Principle 3. Air expanding from higher to lower pressures at the speed of sound extends lift pressures along streamlines, dissipates lift pressures across streamlines, and interacts with air flow to turn streamlines.

These "Three Principles" are stated in terms of continuous mechanics of how air flow interacts with surfaces, but as discussed in this paper, their mechanisms are consistent in both molecular and continuum mechanics. Steady-level aerodynamic lift is created when these principles align to create higher pressures on lower surfaces and lower pressures on upper surfaces.

Here, the "impacting" occurs in an airfoil's boundary layer where air's dynamic pressure (i.e., $0.5\rho U^2$) is transformed from velocity to pressure. This transformation is particularly evident in the forward stagnation point of the airfoil and is a natural fallout of the molecular theory of gases. At the molecular level, "diverging" is the opposite of converging (i.e., impacting), leading to a lower-pressure on surfaces. Once pressure differences are created, dissipation of those pressure differences occurs at the translational speed of gas molecules which manifests as the speed of sound.

These three principles are inherent in solutions to the Navier-Stokes equations but not inherently incorporated into commonly-cited analytically-derived equations for simple explanations of how air flow creates aerodynamic lift.

This paper progresses from a background on the Navier-Stokes equation to results and analysis of CFD analyses of airfoil models for the flat plate, venturi tube, and flat plate enhanced with flaps and slats. The discussion includes an explanation of trends based on the molecular theory of gases, identification of advances in solar aircraft design and ground effect flight enabled by the insight of the three above listed basic-physics' principles, and a brief discussion of commonly used aerospace terms versus the terms used in the Three Principles.

Trends in aircraft research often emphasize boundary layer separation, where the boundary layer is identified as the space next to the surface with typical laminar flow stratification and boundary layer separation is a disruption of laminar flow into turbulent flow. Boundary layer separation is an accelerated form of lift pressure dissipation that is beyond the scope of this work and not necessary in the present text which emphasizes the manner in which lift is generated rather than how lift forces may undergo accelerated dissipation.

2. Background

Authors Suppes and Suppes initiated this work in 2023 with initial versions of the Three Principles published in January of 2024 [1]. This paper pursues a rigor based on molecular mechanisms, continuum mechanisms, extrapolations, and consistency with the Navier-Stokes equations.

Equation 1 presents the Navier-Stokes equation. In the simplest aerodynamic lift application, the objective of solutions to the Navier-Stokes equation is to provide pressure and velocity profiles in the area around an airfoil or the space around a lifting body. A line integral of pressure around the airfoil (2D sectional slice of a lifting surface) can yield lift and drag forces while for a lifting body (3D, i.e. a lifting body like al wing) the surface integral provides the lift and drag forces.

$$\underbrace{\rho\left(\frac{\partial \mathbf{u}}{\partial t}+\mathbf{u}\cdot\nabla\mathbf{u}\right)}_{1}=\underbrace{-\nabla p}_{2}+\underbrace{\nabla\cdot\left(\mu(\nabla\mathbf{u}+(\nabla\mathbf{u})^T)-\frac{2}{3}\mu(\nabla\cdot\mathbf{u})\mathbf{I}\right)}_{3}+\underbrace{\mathbf{F}}_{4} \quad (1)$$

Where **u** is the fluid velocity, ***p*** is the fluid pressure, ***ρ*** is the fluid density, and ***μ*** is the fluid dynamic viscosity.

COMSOL decouples the terms of equation 1 as [2]:

1. Inertial forces
2. Pressure forces
3. Viscous forces
4. External forces

The external forces on airfoil and lifting body analyses are either pressure forces normal to the surface or viscosity forces tangential to the surface.

For the present analysis, the Navier-Stokes equation must be solved under the continuity constraint such as defined by Equation 2. Laminar flow analysis is sufficient for initiation of the present study; including turbulence and boundary layer separation requires additional constraints and respective equations for better representation of fast kinetic systems.

$$\frac{\partial \rho}{\partial t}+\nabla\cdot(\rho\mathbf{u})=0 \quad (2)$$

A typical approach to solving the Navier-Stokes equation in 3D is to generate a 3-dimensional mesh which is solved to provide pressure and velocity as a function of x, y, and z coordinates representing longitudinal, vertical, and span dimensions. The complexity of the solution requires an iterative solution process, typically requiring hundreds of solutions in the mesh space to converge upon a solution.

In the mesh, the lifting body surface is a barrier to both velocity's vector and further changes velocity's gradients with velocity's gradient appearing four times in equation 1. The complexity of the equation in combination with a contoured surface shape does not yield a simple explanation in equation form.

Equation 1 can be simplified under assumptions of: a) 2 dimensions, b) zero viscosity, and c) a mesh location without a surface.

$$\rho\left(\frac{\partial u}{\partial t}+u\nabla \mathrm{u}\right)=-\nabla \mathrm{p} \quad (3)$$

Where:

$$\nabla \mathrm{u} = \begin{bmatrix} \frac{\partial u}{\partial x} \\ \frac{\partial u}{\partial y} \end{bmatrix} \quad (4)$$

$$\nabla \mathrm{p} = \begin{bmatrix} \frac{\partial p}{\partial x} \\ \frac{\partial p}{\partial y} \end{bmatrix} \quad (5)$$

At an airfoil's surface, the velocity normal to the surface is set to zero as a boundary condition. Also, a no-slip constraint is applied setting air velocity along the surface to zero. A pressure force on the surface is equal to the pressure times the area and a viscous force is proportional to the shear in the boundary layer and dependent on the viscosity. An integral of surface force vectors in vertical and horizontal directions will yield a lift equal to the sum of vertical pressure lift and viscous lift as well as a drag equal to the horizontal forces sum as pressure drag and viscous drag.

Airfoil Analysis and Principles 1-3 - Figure 1 provides example pressure profiles generated by a solution of the Navier-stokes equation where higher pressures are red and lower pressures are blue with the lime-green color being background pressure, referred to as free-stream pressure. The highest-pressure and lowest-pressure regions of Figure 1 vary in shape from circular to semi-circular. These shapes are a result of flow impacting or diverging from the surface to generate higher or lower pressures followed by the rapid dissipation of those peaks in magnitude where the surface blocks dissipation into the surface, resulting in circular to semi-circular shapes.

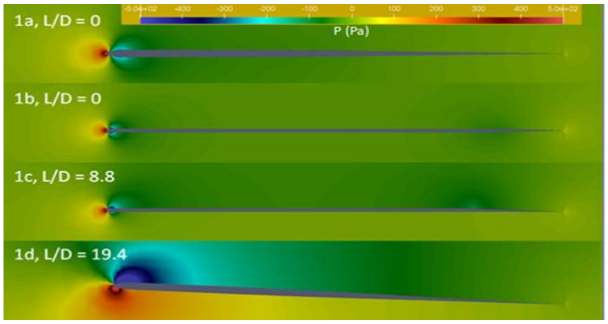

Figure 1. Pressure profiles on airfoils that illustrate key aspects of how aerodynamic lift is generated [3].

Term 2 of the Navier Stokes equation (Equation 1) identifies the pressure gradient as a driving force for change. More specifically, in the context of Equation 1 pressure gradients are a driving force for changes in velocity. For airfoils and respective lift pressures, the objective is to create higher pressures on lower surfaces and lower pressures on upper surfaces. Dissipation normal to the surface reduces lift pressures while dissipation tangential to the surface can increase lift forces. The pressure force term is the mathematical manifestation of Principle 3.

Pressure differences expand of the speed of sound as identified in Principle 3. Abbott identifies this in a chapter on compressibility at subsonic speeds [4]; however, the Navier-Stokes equation does not limit the impact of pressure gradients to compressible fluids. Figure 1 data were generated using a CFD as an incompressible fluid, and yet, clearly show dissipation of pressure gradients lateral to sources of generation.

The Term 1 inertial forces provide a mathematical expression of Principles 1 and 2. A common feature of all airfoils generating aerodynamic lift is the leading-edge stagnation point, named after the stagnation of air flow at the leading edge [5]. The leading-edge stagnation point is also a maximum for pressure and typically approaches the dynamic pressure of oncoming air relative to the airfoil. Air above the stagnation point flows above the airfoil; and air below the stagnation point flows below the airfoil.

Kinetic energy of air flowing on the streamline ending at the stagnation point is transformed to pressure, with the streamline typically terminating near the leading edge of the airfoil. It is a matter of semantics as to whether the air stagnation streamline is considered to "impact" the surface versus the air's translational vectors becoming more random in direction before impacting the surface after the molecules collide in the pressure field that forms over the leading edge. For lack of a better concise term, the term "impact" is used with Principle 1. Increased momentum from air's molecules causes the increase in pressure, and that increased momentum originates from the flow of air toward the surface.

Stagnation regions are not stagnant air; rather, they are steady-state phenomena with air entering at a leading surface and exiting at a trailing surface. Air's energy transforms from velocity to pressure as it enters the stagnation region and from pressure to velocity as it exits the stagnation region. The transformations are at the molecular level and include molecule-surface collisions.

For streamlines above the leading-edge stagnation line, the pressure forces of the leading-edge stagnation region to join with the inertial forces, in a conservation of momentum, to form streamlines that do not intercept the leading-edge surface.

In addition to a leading-edge stagnation point, airfoils typically have a trailing edge stagnation point at the trailing edge with several illustrated by Figure 1. The higher pressures of the trailing edge stagnation point are a result of air flow from above the airfoil impacting air flow from below the stagnation point. In well-developed pressure profiles, the pressures of leading-edge and trailing-edge stagnation point expand (Principle 3) to form higher pressures throughout the lower surface.

Principle 2 is a process opposite Principle 1 where air's flow depletes air adjacent to the surface in streamlines that gradually increase in distance from the surface in the direction of flow. The topic is discussed in the results section in terms of the molecular theory of gases [6-9].

While Principles 1-3 can be substantiated based on published materials, a further exemplification is warranted through experiments targeting further elucidation of the physics behind the principles. A discussion then relates the principles to the kinetic theory of gases and broader concepts of reversibility in generating aerodynamic lift. An improved understanding of reversibility in generating aerodynamic lift enables a system's-level analysis of performance with identification of approaches to improve lift-drag ratio (L/D) efficiency.

Turbulence and Boundary Layer Separation – Turbulence results in lost work due to irreversible mixing; in the case of turbulence around airfoils, the lost work is the result of higher pressures mixing with lower pressures. Turbulence and boundary-layer separation led to the deterioration of aerodynamic lift pressures; they are contrary to the generation of aerodynamic lift. The work of this paper sets the foundation for further discussions on boundary-layer separation; however, the topic of boundary layer separation is outside the scope of this paper.

From a simplified perspective, traditional systems level analyses implicitly recognize that viscous losses are a form of lost work. Other forms of lost work such as expansion of pressure between adjacent streamlines is not considered in schools of thought like Bernoulli's theory of lift.

3. Methods

OpenFOAM CFD software was used to simulate digital prototypes prepared as STL files. Two-dimensional (2D) simulations were used to identify trends in performance while 3D simulations were performed on the final prototypes. Unless otherwise reported, the scale chords of the STLs were 1 m, the fluid was air at 1 atm pressure, and the free stream velocity was 40 m/s. A RANS "k-ω SST" turbulence model was used with OpenFOAM solver at air's standard temperature and pressure.

Model airfoils of a flat plate, the venturi tube, and a flat plate enhanced with flaps and slats were simulated using turbulent flow models with laminar models for both the flat plate and venturi tube as well. The latter model was simulated in ground-effect flight. The CFD results are evaluated using three basic principles of physics and compared to the most common theories of lift.

For ground effect simulations, the ground was simulated as a lower boundary condition with a velocity equal to the free stream air. Unless otherwise identified, the propulsion sources were rectangular with a height of 2 cm and thickness of 2 mm with specification of velocity of these cell zone velocity sources in m^4/s^2. Free steam flow boundaries were simulated at a minimum of 5 chord lengths from the vehicle in free stream directions.

The experimental investigation consisted primarily of computational fluid dynamic (CFD) studies of 2D airfoils. Results of an example 3D digital prototype are presented in the discussion section to validate how 2D airfoil results can identify how to achieve good performance in a 3D digital prototype which transforms the results from an airfoil only theory to practical results on aircraft design.

When simulating aerodynamic lift, the simulations are for result convergence at steady-state and level flight. All simulations are based on models near one meter of length in the direction of flow where for the conditions of this work the results varied little for changes of at least an order of magnitude in the Reynold's number.

The results and discussion advance frontiers useful in education and new aircraft designs with simple structures and novel airfoils, and as such, vary from available benchmarks to validate high accuracy of simulations. On the frontiers of education level, consistency at molecular, continuum, and extrapolated levels is discussed as a validation. Simulations are consistent with common benchmarks in free flight but vary from those benchmarks on the topics of using the pressure fields around propulsors to improve performance and using the ground to block the downward dissipation of lift pressures. The discussion refers to other papers on digital prototype performances which provide additional comparisons for simulation conditions and method validation.

4. Results

Asymmetric Flat Plate - Figure 1 presents the pressure profiles of a vertically-symmetric airfoil and an asymmetric variation (Figure 1c) to illustrate how lift pressure regions are created on surfaces by aerodynamic forces. Proceeding from the leading edge to the trailing edge on the symmetric airfoil at zero pitch (Figure 1a): i) air at free stream velocity impacts the leading edge to create a forward high-pressure region "*The forward high-pressure region has historically been referred to as a "forward stagnation point"; however, the important feature of the region is the higher pressure and not stagnation.*"; ii) a low-pressure area forms behind the leading edge as the result of upward expansive flow from the forward high-pressure region joining with oncoming airflow to form a resultant momentum vector that diverges from the surface; iii) the resulting low-pressure region pulls air back towards the surface, increasing pressure behind the lowest pressure region, iv) subsequent airflow balances the tendency for air to flow straight/parallel versus turning to follow surface curves, and v) behind the trailing edge, velocity streams from upper and lower surfaces collide to create a region of higher pressure immediately behind the trailing edge.

When the surface of the airfoil is flat, air eventually achieves a flow parallel to the surface, and pressure approaches the free stream value until the surface tapers to the trailing edge point (see Figure 1b). An asymmetry in the trailing section taper (Figure 1c) results in the formation of a trailing-section low-pressure region—that low-pressure region impacts pressure throughout the airfoil, producing an increase in ***L/D*** from 0 to 8.8. Due to air's expansion at the speed of sound, a trailing section lower pressure region formed by diverging air flow overcomes oncoming velocity in subsonic flight to impact pressure throughout the airfoil's surface. The term "expansion at the speed of sound" refers to the manner in which air molecules at a higher pressure mix with surrounding lower-pressure air at the translational speed of air molecules, which inherently defines the speed of sound. The expression is utilized as a commonly known convenient and accurate reference for the rate as which these phenomena develop. The impact of the trailing taper is increased by positioning of the trailing-edge stagnation point below the lower surface, enabling direct expansion of the pressure forward along the lower surface.

Figure 1d illustrates how a change in airfoil pitch causes more air flow to diverge from upper surfaces and more air flow to converge on lower surfaces to create lift; an increased pitch creates more lift at the lower velocities for takeoff and landing. While ***L/D*** is typically not a strong function of velocity, the lift and drag are functions of velocity. A disadvantage of using airfoil pitch to generate greater lift is the resultant increase in airfoil surface area with pitch angles greater than 2°, resulting in a lower ***L/D,*** which decreases overall airfoil efficiency**.**

When at sufficient magnitude, the lower-pressure region draws air from surrounding streamlines; this changes air's angle of attack ("AoA") at the leading-edge, moving the leading-edge higher-pressure region aft-ward towards more-horizontal surfaces. Here, AoA refers to the angle of attack on the surface versus the more-common application where AoA is the angle of frees stream velocity vectors relative to the pitch of the airfoil's chord. This transformation is a key feature of airfoils achieving ***L/D*** greater than 40:1. The highest ***L/D*** are a result of reduced drag versus increased lift; reduced drag occurs when induced thrust at the leading-edge cancels the drag of the remaining airfoil surfaces. The term "induced thrust" refers to surface-pressure interactions that lead to a forward force, generally on the underside of the leading edge for airfoils concave upward, in contrast to induced drag which refers to surface-pressure interaction that leads to an aft-ward force direction.

Figure 2 provides an exaggerated version of the flat asymmetric airfoil for the purposes of illustrating how momentum vectors merge (Figure 2b), velocity profiles (Figure 3), and streamline paths (Figure 4). Velocity vectors merge with conservation of momentum to form resultant vectors.

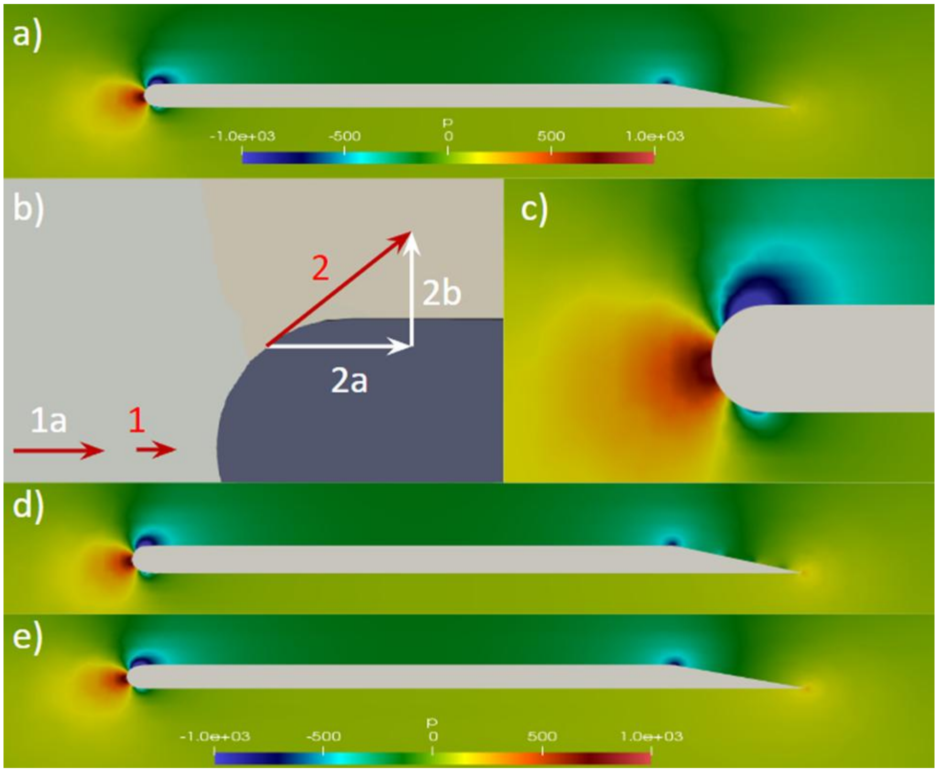

Figure 2. Pressure cascade for generating aerodynamic lift. Pressure profiles of an expanded view of asymmetric flat plate airfoil illustrating pressures generated as a result of i) air impacting leading edge and ii) resultant velocity vector of free stream and expanding air. The profiles are for turbulent air (a and c), air without turbulence simulation (d), and ideal-gas air without turbulence or viscosity (e).

A comparison of flat plate pressure profiles for turbulent, laminar, and near-zero viscosity laminar flow is provided by Figures 2a, 2d, and 2e and is summarized by Table 1. Laminar flow creates the greatest reduction in drag while viscosity has a greater impact on increasing lift while further decreasing drag. The higher L/D of laminar flow can be attributed to the stronger trailing-edge inflection point which increases pressures throughout the lower surface. These trends validate applicability of equation 3 where primary mechanisms for generating high lift are pressure gradients from laminar flow while turbulence is primarily a mechanism through which lift pressures dissipate and L/D reduces.

Table 1. Impact of turbulence and viscosity on aerodynamic lift at low Reynolds number asymmetric flat plate airfoil. *viscosity is set to 1e-15 to simulate zero viscosity.

Model	L/D	$C_{L\ pressure}/C_{L\ viscous}$	$C_{D\ pressure}/C_{D\ viscous}$
Turbulent k-ω SST	18.7	4617	2.28
Laminar	24.5	5320	9.24
Laminar, zero* viscosity	30.7	N/A	N/A

The velocity profiles of Figure 3 identify turbulence on the back half of the upper surface of the trailing taper for the simulation including turbulence. What appears as turbulence at the trailing edges of the laminar and low viscosity models is likely solution instability which identifies the turbulent model is the most accurate model. However, the following trends between models provide insight and are consistent with the underlying physics:

- Increasing turbulence and viscosity increases viscous drag as identified by increasing values of the ratio of pressure drag to viscous drag of Table 1.
- Pressure effects dominate L/D with the primary impact of eliminating turbulence at these conditions being reduced drag on the trailing taper.

These trends would not persist as velocity increases with increased boundary layer separation.

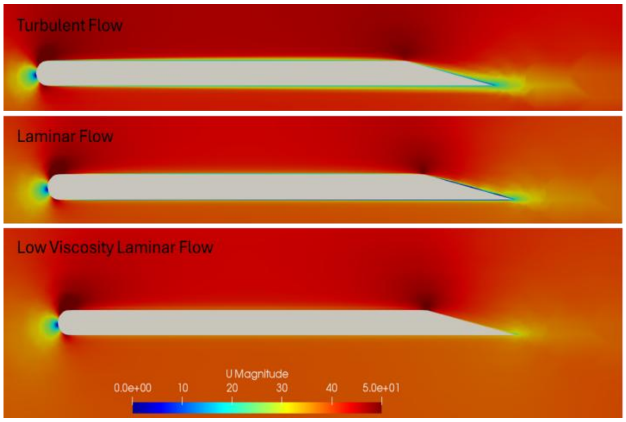

Figure 3. Velocity profiles for flat plate airfoil of Figure 2.

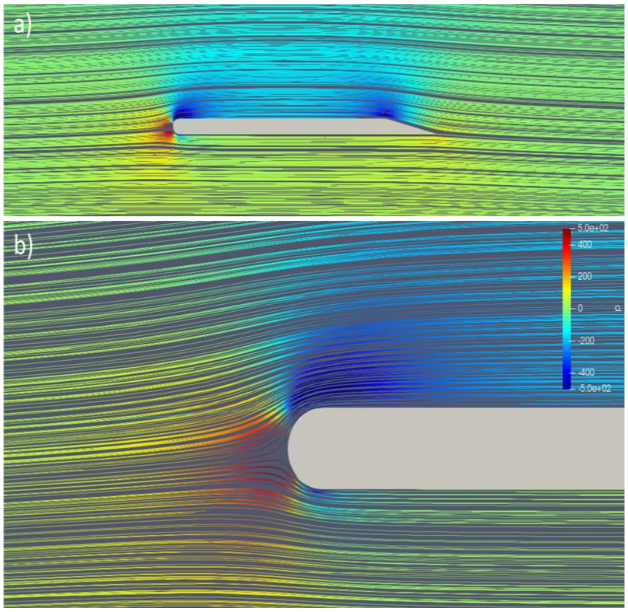

Figure 4. Streamlines overlaying pressure profiles for the simplified design of Figure 2.

Flat Plate with Flap and Slat Options - Figure 5 summarizes pressure profiles of a flat plate with and without: ground effect, a flap, and both a flap and a slat. Each of the airfoils of Figure 5 have the characteristic leading-edge stagnation point and low pressure immediately behind the leading edge due to flow diverging from the surface.

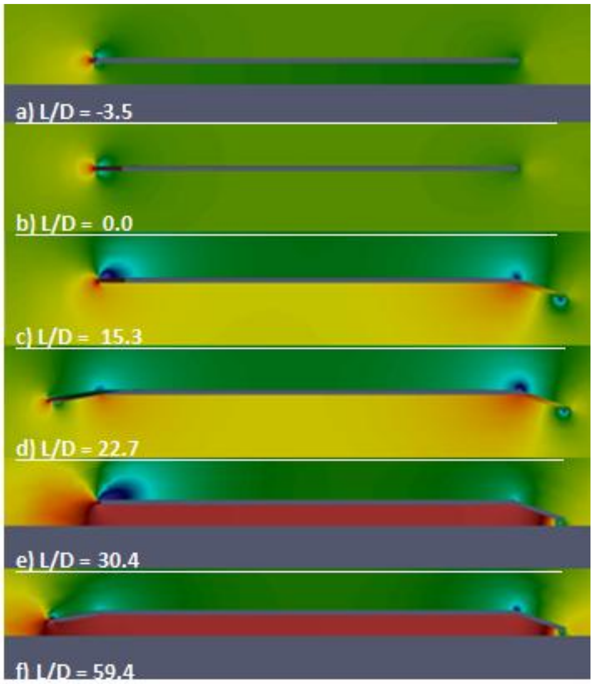

Figure 5. Pressure profiles of a flat plate airfoil with slat and flap options presented from lower to higher L/D.

Ground effect is a recognized flight phenomena where flight in proximity to the ground has been observed to increase lift and L/D flight efficiency [10-13]. An anomaly to this trend is the symmetric flat plate which has a higher L/D of 0 when distant from the ground versus L/D of -3.5 when close to the ground. The negative lift and L/D when close to the ground is the result of a negative lower pressure region forming at the leading section of the lower surface with a rearward influence.

The remaining airfoils (Figure 5c-5f) has a trailing flap. The trailing flap exhibits a lower pressure on the upper surface, similar to the asymmetric taper of Figure 4. In addition, air impacts the lower surface of the flap, generating a higher pressure. As a result, the method in which the Figure 4 asymmetry is expressed throughout the surface of the airfoil is exasperated by formation of higher pressure on the lower surface and lower pressure on the upper surface. As a result, the flap's impact overwhelms the phenomenon exhibited by Figure 5a.

A comparison of Figure 5c to Figure 5e illustrates how, as the ground is approached, the ground becomes more effective in blocking the downward dissipation of lift pressures created by the trailing flap and expanding forward at the speed of sound.

The forward slat further increases L/D efficiency by creating additional air flow divergence on the upper surface. Also, the forward slat exhibits a phenomenon referred to as "induced thrust". Induced thrust refers to a pressure interaction with a surface that creates a forward-directional force on the airfoil. The forward slat has higher pressures on the lower surface and lower pressures on the upper surface; both leading to induced thrust. Induced thrust subtracts from drag in L/D efficiency. And so, as L/D efficiency increases, induced thrust is the most-effective mechanism to further increase L/D, often with resultant L/D >40.

The Figure 5 simulations are 2D, and so, are not capable of simulating wingtip vortices. Hence, the ground effect enhancements are independent of the absence or presence of wingtip vortices.

The Venturi Restriction - Figure 6 illustrates three cases of flow through a venturi tube which will be interpreted using the Bernoulli theory of flight, a traditional simple explanation for aerodynamic flight.

A comparison of venturi tube pressure profiles for turbulent, laminar, and near-zero viscosity laminar flow is provided by Figure 6. The CFD results identify a solution instability after the restrictions which persists independent of viscosity and turbulence. This instability goes away with the Figure 7 CFD profiles for a tube without an increase in area after the restriction where CFD convergence occurs to better-validate findings.

In physical processes, fluid compressibility can act as a buffer of energy in the gas phase transfer of energy. The incompressible assumption of the solutions of Figure 3 and 6 do not have this buffer, but the numerical CFD solution process is still able to arrive at solutions. In an absence of a stabilizing buffer, the solution for parts of the profile can oscillate between unstable states without convergence to a stable solution.

A comparison of Figure 6 to Figure 7 profiles from the entrance to the minimum restriction reveals a lower pressure at the minimum restriction for the full venturi tube. This lower restriction can be attributed to the divergence of flow from the edge after the minimum diameter creating lower pressures (Principle 2) and with expansion of pressure (Principle 3) extending the impact of that lower pressure forward through the tube.

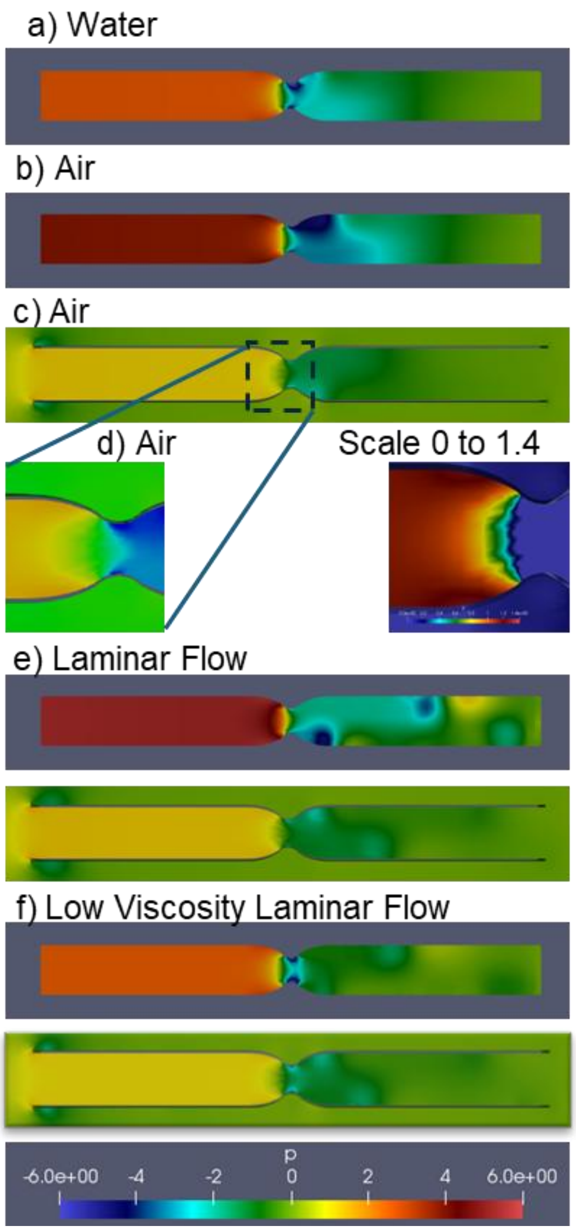

Figure 6. Pressure profiles of 2D CFD simulation of water and air flowing through a venturi restriction with 2 m/s velocity forward boundary conditions. Here; a) water and b) air are flow within a tube with a set velocity inlet condition and free stream pressure outlet, while c) is a for a tube in a 2 m/s free stream air flow. d) is the image "c)" profile at a different pressure scale, e) depicts laminar flow for air through the closed and open tube systems and f) depicts low viscosity laminar flower through the closed and open tube systems.

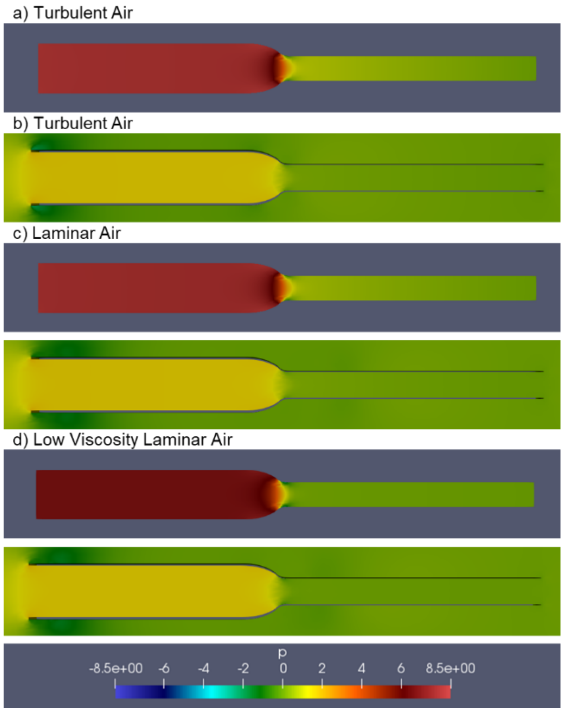

Figure 7. Pressure profiles of 2D CFD simulation of air flowing through a half-venturi restriction with 2 m/s inlet velocity condition which does not expand after the constriction. a) is flow in a closed system tube with pressure boundary condition at the exit, b) is a for a tube in a flow of 2 m/s free stream air, c) is for laminar flow through the two tubes, and d) is for low viscosity (1e-07) flow through the two tubes.

The Bernoulli equation identifies that when energy is conserved in an incompressible fluid system, higher pressures can be transformed into higher velocities. While energy is transferred between velocity and pressure terms, the process occurring in the venturi tube is more complex.

The simple application of the Bernoulli equation fails during the initial 20% restriction in diameter where velocity increases but pressure does not decrease. In this region before the inflection point of the diameter (as a function of length), velocity momentum is expressed on the wall of the tube. The increase in pressure before the inflection point is better exemplified by the expanded scales of Figure 6d.

The explanation for this pressure increase resides in the fundamental mechanism of how a fluid interacts with a curved wall to turn and follow the wall. That fundamental mechanism includes the following steps:

1. At a thin boundary-layer level, fluid flow impacts the surface where the fluid's velocity is converted to higher pressure. Noteworthy is that the velocity on the surface is zero, and so, Bernoulli's equation is followed where decreasing velocity results in higher pressure.
2. The higher pressure in that thin boundary-layer expands at the speed of sound. For the initial restriction, higher pressure expands to rapidly for a steady-state of near-constant pressure throughout the space forward the restriction.
3. Flow patterns develop with flow parallel to the wall (for laminar flow), where after the diameter's inflection point, the flow diverges from, rather than impacts, the wall. At this point, lower pressures are formed at the surface with a rapid dissipation into a bulk flow pressure.

Hence, it is understandable that the venturi tube appears to simply follow Bernoulli's theory, but the actual phenomena are more complicated as explained following Principles 1-3. Energy is transformed between pressure and velocity, but momentum transfer of air molecules with the surface are the fundamental source of changes in pressure.

The interaction of expanding pressure and flowing fluid follows the law of the conservation of momentum. As a consequence, expanding pressure changes the velocity vector of the flowing air; the expansion of pressure "turns" the air to follow the contour of the tube. A widely-used theory of aerodynamic lift is the "turning air theory" where the momentum of turning air is attributed with generating lift pressures; when in fact, the pressures generated by basic physics (i.e., Principles 1-3) are the fundamental cause of turning of air.

For a Venturi tube in free stream flow, the "expansion of pressure at the speed of sound" extends to the tube entrance as evident by the observation that the pressure in the first half of the tube is higher than free stream pressure (See Figure 7). The higher pressure at the entrance acts upon approaching free stream flow to divert part of the flow around the tube rather than through the tube; hence, the higher pressure in the first half of the tube in free flow is lower when exposed to a free stream than for the Figure 6a benchmark. For the second half of the tube in free stream flow, free stream pressure extends/expands into the tube from the tube exit. The free stream acts as a reservoir of pressure that essentially established a tube-effluent boundary condition.

A comparison of turbulent, laminar, and zero viscosity flow in the venturi tube reinforces the earlier conclusions from the comparison of these conditions over the flat plate.

The conclusion from a critical analysis of the Figure 6 pressure profiles is that even within the classic time-tested Venturi tube example, the simple explanation of Bernoulli's equation breaks down. The basic concepts of energy conservation persist, but the assumptions in the derivation of Bernoulli's equation create substantial error when air interacts with surfaces. Common applications of Bernoulli's equation account for friction from viscosity, but they do not account for pressure created by impacting and diverging of air flow with surfaces. The deviations from ideal venturi tube behavior are further exemplified by Figure 8 which compares pressure profiles as the minimum diameter is approached by the flow. The impact of pressure generation due to the flow's momentum expressed on the surface is clearly expressed for both the full venturi tube and the half-venturi tube. Ideal venturi tube flow has a substantially different pressure profile. The scales were adjusted to emphasize these differences. The magnitude of pressure change as the diameter lessens varies from 8 to 5.5 to 2.25 for the full, half, and ideal tubes respectively. The full tube has the greatest range in pressure since the expansion after the minimum in restriction further decreases pressure due to Principle 2 diverging of flows. Both the have increases in pressure from flow's momentum expressed during the restriction before the inflection point of the decreasing diameter. The ideal flow does not have a mechanism to interact with the surface as provided by the Navier-Stokes equation.

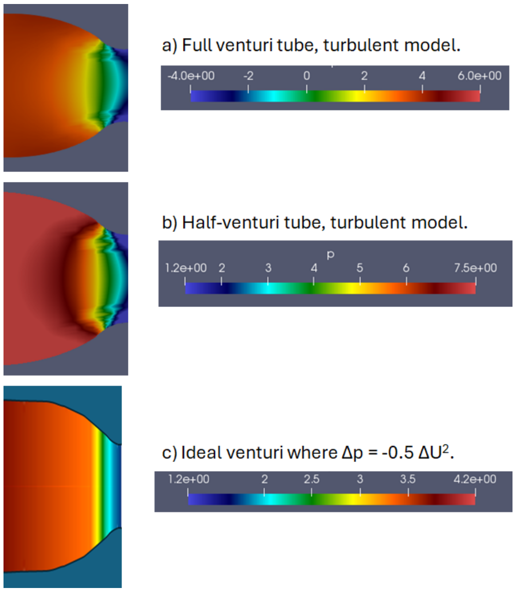
a) Full venturi tube, turbulent model.

b) Half-venturi tube, turbulent model.

c) Ideal venturi where $\Delta p = -0.5\ \Delta U^2$.

Figure 8. Expanded views and scales of pressure profiles a venturi restriction with feed at 2 m/s. While referred to as tubes, the 2D simulations are properly characterized with a height rather than a diameter. Redo middle graph with 8.0 as upper scale.

5. Discussion

The pressure profiles demonstrate the following:

1. The generation of lift pressures on the airfoil's surface due to air flow converging toward or diverging from the surface.
2. Pressure expanding from higher to lower pressures:

- consistent with Term 2 of the Navier-Stokes equations,
- consistent with basic physics,
- to extend lift pressure along the surface of the airfoil, and
- to dissipate lift pressure normal to the surface of the airfoil.

In the case of ground-effect flight, the results illustrate how the ground blocks the downward dissipation of lift forces.

Theories of lift like Bernoulli's Theory of lift fail to account for the importance of how pressure can expand to increase lift ("lift pressure extension") and dissipate to reduce the impact of otherwise effective generation of lift forces. In general, the past century's hundreds of papers and books advancing analytical explanation of aerodynamic lift fail account for the importance of lift pressure extension and dissipation [4, 5, 14-17]. These past theories also fail to identify the fundamental causality that causes advantageous flow patterns and pressure profiles. The simple explanation for these omissions is that the results justified the means, and the results appeared to be accurate.

The Results identifies air flow converging toward or diverging from the surface as the fundamental causality. A discussion of streamlines provides further insight of engineering significance.

Streamline Interpretations – The first key aspect of generating aerodynamic lift is the transformation of air's dynamic pressure into static pressure at the leading edge of the airfoil. While the higher-pressure region directly produces drag, it also initiates the dynamics that can generate lift forces throughout the airfoil.

For Figure 4 streamlines near the upper surface, a volume of gas approaching the airfoil undergoes energy transformation of the Equation 6 energy balance.

$$\text{Accumulation}=\text{Energy In}-\text{Energy Out}+\Delta KE+\Delta\Phi+H+W_s \quad (6)$$

where:

KE is kinetic energy,

Φ is potential energy,

H is enthalpy, and

W_s is shaft work, where enthalpy is equal to internal energy plus the product of pressure and volume (by definition) and accounts for PV work done on the fluid.

Within the constraints of the Equation 6 energy balance:

1. The pressure increases and velocity decreases as the air molecules have an increased frequency of collisions as the airflow enters and contributes toward the forward higher-pressure region. At subsonic airflow velocities, the velocities of the molecules are faster than the airflow velocity, and so, the higher-pressure region extends in all directions from the leading edge except as blocked by surfaces.
2. In a flow velocity resultant from the airflow vector combined with a higher-pressure expansion [flow] vector, a resultant velocity vector having a negative pitch angle emerges (Figure 2b exemplification).

Resultant vectors for streamlines closest to the leading-edge impact the surface, which increases pressure, while resultant vectors progressively further from the leading-edge diverge from the surface and reduce surface pressures to produce a region with pressures lower than free stream pressure.

1. Air flows encounters pressure gradients (a lower pressure region next to the surface) that contribute a flow towards the airfoil surface, with the resultant airflow vector having an incrementally increased (less negative) pitch.
2. This process of airflow vectors being adjusted by pressure gradients continues throughout the chord dimension of the airfoil. The impact and divergence of airflow vectors with the surface also continues along the chord dimension.
3. A curvature and/or change in the airfoil surface affects impacting and diverging air flows with the corresponding incremental increases or decreases to surface pressures.
4. Behind the trailing edge of an airfoil, upper and lower airflow vectors collide to cause a higher-pressure region immediately behind the trailing edge.

Surface pressures on an airfoil create pressure gradients that effectively "Turn" airflow. Hence, the Turning Air Theory incorrectly attributes turning air as the cause of lift pressures [18]. On the contrary, pressures on an airfoil surface create pressure gradients that turn the airflow. The Turning Air Theory both confuses cause with effect and is primarily an empirical correlation.

Boundary Layer – As a correcting detail, the only air streamlines that converge toward or diverge from surfaces are those streamlines within a thin boundary layer. The only streamline that actually collides with the surface is the leading-edge stagnation line terminating in the leading-edge stagnation point. Beyond that boundary layer, molecule-molecule collisions in the gas phase transfer pressures and form "pressure fields" in the boundary layer where air flow transforms to pressure and pressure transforms to velocity.

Reversibility of Streamline Paths – For a streamline about 0.1 t (thickness) above the airfoil, the following occurs from an energy balance perspective starting as the air approaches the leading section of the airfoil:

1. Gradients of increasing pressure are crossed, converting kinetic energy into pressure energy (i.e., pressure energy is stored as PV (Pressure times Volume) and is typically included in enthalpy terms of energy balances).
2. Gradients of decreasing pressure are crossed, converting pressure energy into kinetic energy.
3. Gradients of increasing pressure are crossed, converting kinetic energy into pressure energy.
4. The process is repeated throughout the chord dimension until pressure gradients are negligible.

The air in the streamlines has the critical role of storing and releasing energy in the forms consistent with the steady-state sustainment of the surface pressures. Furthermore, the transformations within the Equation 6 energy balance along the streamline path are mostly reversible in nature. Hence, the energy balance, as applied to the streamline, identifies a series of stages that reversibly "sustain" the pressure of aerodynamic lift—analogous to how the gas working fluid in a heat engine cycle stores and releases energy.

Aspects of flow that improve streamline reversibility include:

1. Laminar flow patterns instead of turbulent.
2. Streamline conditions immediately aft the airfoil that are the same as free stream conditions.

Both of these relate to the absence of boundary layer separation and turbulence. The latter of these, as well as the stages of the streamline, do not identify downwash as being necessary to generate lift, which appears to be accurate for steady-level flight. This conclusion identifies an error in momentum theories of steady-level flight that rely on downwash to generate steady-level lift.

This approach to reversibility of lift generation sets the foundation for a system-level analysis of aerodynamic lift using the control volume summarized in Figure 9. Only the aft surface of the control volume deviates from free stream conditions, and so all the information needed for a system-level analysis of lost work (i.e., available energy analysis) can be obtained from the temperature, pressure, and velocity vectors of the air aft the trailing edge. If pressure gradients exist between the aft-vertical-cross-section of air to or from the airfoil, further critical analysis of how those gradients may have an aft-extending influence on the airfoil's aerodynamic lift is needed.

The term "boundary layer separation" refers to the formation of turbulence on a wing's upper surface which results in losses of lift. Much aerospace research has a focus on understanding boundary layers due to the manner in which the emergence of turbulence (i.e., boundary layer separation) can result in significantly diminished aerodynamic lift. Turbulent flow generates more shear drag than laminar flow; however, shear drag tends to be at least an order of magnitude less than form drag for aircraft which points toward form drag as the culprit of sudden losses in aerodynamic lift with boundary layer separation.

Reduced aerodynamic lift from the turbulence of boundary layer separation is the result of two phenomena:

- The mixing of streamlines is an irreversible process rapidly dissipating the lowest upper surface pressures and nullifying the spreading of the lower pressures along the upper surface.
- By destroying a laminar flow along the upper surface, turbulent flow destroys the trailing edge stagnation point and rather than higher pressure from the trailing-edge stagnation point extending along the lower surface, a lower pressure region extends along the lower surface destroying lower surface lift pressures.

Table 1 provides data in further support of these conclusions.

The transformation of velocity and pressure is included in Equation 6 in the enthalpy term, and is important in the dynamics of how air flow generates aerodynamic lift. However, the mechanisms through with lift forces are generated and dissipated between boundary layers includes more than the Equation 6 energy balance. Viscosity losses ultimately show up in the internal energy component of the enthalpy terms of Equation 6.

Viscosity tends to have minimal impact on lift. The impact on drag under two circumstances: a) when turbulence develops and b) when induced thrust cancels most of the form drag from the airfoil shape. Induced thrust can be created by a propulsor;, and when created by a propulsor, the gain in induced thrust versus lost in momentum-based thrust from the engine reduces as engine power increases. Any reduction in total drag from surfaces beyond the airframe's form drag has a 1:1 gain:loss ratio with the engine's momentum-based thrust.

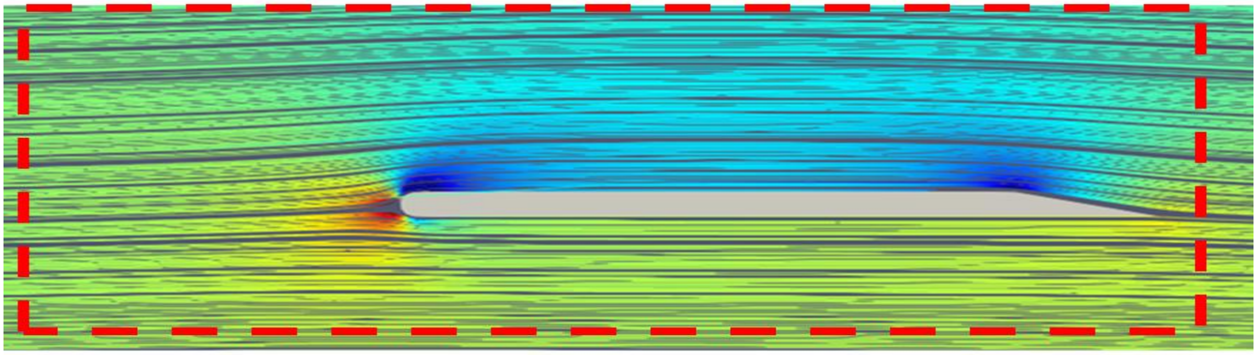

Figure 9. Control volume for system's level analysis of an airfoil.

Kinetic Theory of Gases – The continuum-level Principles 1-3 are validated on the discrete level of gas molecules through the following restatements in terms of the kinetic theory of gases:

Heuristic 1. Air molecules having random translational directions have increased velocities relative to an approaching airfoil; therefore, the momentum of the molecules relative to the leading edge are increased by a value proportional to the approach speed with a corresponding increase in force caused by the indirect impact of those molecules on leading surfaces. Here, indirect refers to the manner in which flow momentum is transformed to pressure as it approaches a surface through molecular-molecular collisions Stated in terms of continuum mechanics, *impacting flow causes higher pressures*.

Heuristic 2. In the absence of translational movement of air molecules, an airfoil would create a perfect vacuum in its wake—similar to the way a snow plow leaves a cleared snow path in its wake. In practice, gas molecules flow into the wake and convert that "perfect vacuum" into a lower pressure region, like a sauce filling the void behind a spatula scraping a pan. Stated in terms of continuum mechanics, diverging flow causes lower pressures.

Heuristic 3. At room temperature, gas molecules translate 500 m/sec in random directions; the speed of sound in a gas 340 m/sec which is the conversion from random to directional transit. Thus, gases have a net flow through pressure gradients at about the speed of sound. Stated in terms of continuum mechanics, air flows from higher to lower pressures at the speed of sound.

These heuristic-level verifications can become quantitative through Monte Carlo simulation which is computationally intensive and outside the scope of this paper [6-9].

Overcoming Paradigms – The Turning Flow and Bernoulli theories of flight implicitly teach toward using wings with an emphasis on lift generation on the curved upper surfaces of wings. Lift is a fundamentally a force from the difference of forces acting on the lower and upper surfaces. Ground effect flight is a burgeoning topic where a lift is enhanced by the ground/water blocking the dispersion of higher pressures on lower surfaces.

Ground effect aircraft are poised to redefine maritime transport with Airfish 8 and Regent planned to enter service in 2025 and 2026 at Singapore, Hawaii, and Florida [19, 20]. These aircraft realize efficiencies approximately 25% more than contemporary counterparts in the same size category due to water ground effects blocking lift pressures losses during flight a few feet above water's surface. Recent 3D CFD simulations have identified that more than 100% increase in efficiency is possible when designing based on conservation of lift pressures on lower surfaces of lifting bodies rather than turning of air above wings.

Figure 10 illustrates the pressure profiles of an airfoil as a function of distance from the ground. Lift pressures on lower surfaces dominate performance as the ground is approached, and those lift pressures are primarily a result of expanding pressure from the forward high-pressure region and a trailing flap. For 3D digital prototypes, performance is dominated by the generation of pressure that expands into a lower cavity and the blocking of that pressure loss with side fences, a trailing edge flap, and the ground.

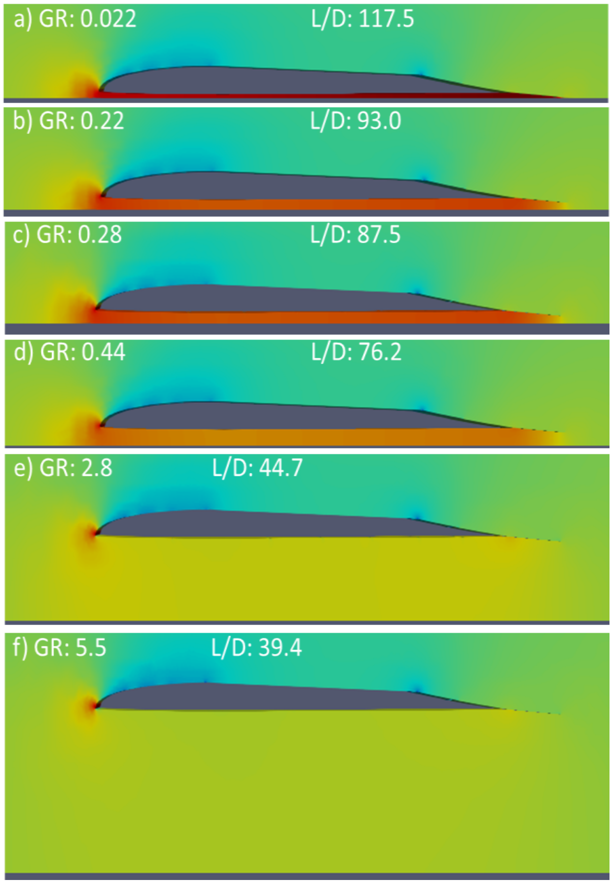

Figure 10. Impact of Ground ratio on the airfoil efficiency. 6.4m airfoils, including trailing flap at 40 m/s with a t/c od 0.064. From a-f), gap ratios are 0.022, 0.22, 0.28, 0.44, 2.8, and 5.5. Ground ratio is ratio of the distance from the ground divided by the height of the airfoil.

In ground effect flight, the ground blocks the downward dissipation of lift pressures. Past simple explanations of aerodynamic lift fail to identify the significant increases in L/D efficiency that are possible through the inclusion of structures (i.e. ground) near the airfoil. A separate paper on optimizing ground effect flight transit (GEFT) provides increasing detail on how to focus lift pressures to generate high L/D efficiency [21-23]. The approach progresses from an explanation of how aerodynamic lift is generated to how to design surfaces to generate high L/D efficiency through Principles 4-6 as follows:

Principle 4. The L/D of a section of an airplane surface is approximately equal to 57° divided by the pitch of the surface in degrees for lower surfaces and -57° divided by the pitch for upper surfaces. The pitch angle is relative to horizontal with the nose up as positive.

Principle 5. Surfaces can be used to block loss of lift pressures leading to increased L/D. Example surfaces are winglets on wings and fences under lifting bodies.

Principle 6. For a ground-effect aircraft with properly-designed lower fenced cavity, 3D CFD estimates of cavity lift pressures are able to approach 2D estimates, enabling 2D airfoil simulations to accurately predict actual performances in many applications.

Impacting Air Flows – Aerodynamic engineering places a high emphasis on the manner in which air flows around bodies rather than impacting materials, and flow streamlines around airfoils clearly identify a prominence of flow around materials. While subtle relative to flow around bodies, impacting flow is a primary causality for generation of lift pressures per Principle 1.

Leading edge stagnation points of airfoils are singularities where, in limit of pure laminar flow, a stagnation line of very low flow rate separates the streamlines flowing over a body from the streamlines flowing under a body. The increasingly low flows of the stagnation line are at steady-state conditions where much of the flow's velocity entering the stagnation regions is transformed to pressure while pressure is transformed to velocity for flow exiting the region. The Figure 11 illustrates what happens at the molecular level.

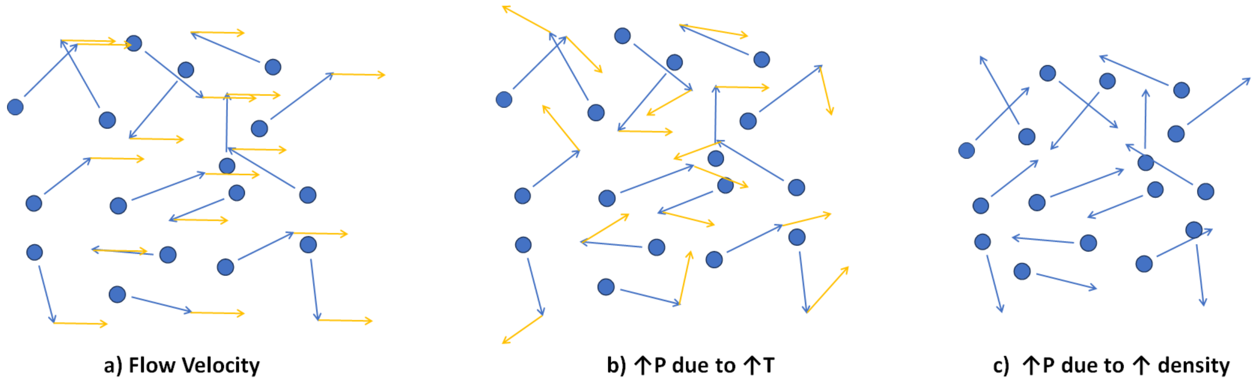

Figure 11. Molecular expression of flow velocity, higher pressure (P) due to higher temperature (T), and higher pressure due to higher density.

As illustrated by Figure 11a, a fluid flow velocity is relative to a body, where in the absence of the body translational velocities of molecules are random in direction. In the presence of the objective the same velocity vector addition to each molecule accurately illustrates a flow velocity relative to the body.

An increase in pressure may be due to any combination of increased temperature (Figure 11b) or increased density (Figure 11c). The following are instances of how impacting flow transforms to increased pressures:

a) Velocity flow impacting a higher-pressure region (i.e. a pressure field) leads to an increase in the random nature of molecular translational velocities which is a transformation from continuum level kinetic energy to pressure.

b) Impacting of air flows of different vectors directions lead to molecular-level collisions that lead to more-random velocities and higher local density which is expressed as higher pressure.

c) A velocity flow impacting a surface transforms constant-direction vector additions at the molecular level to a random-direction vector additions, where it should be noted that a molecules angle of incidence does not survive a collision with a surface verified by the widely-accepted no-slip boundary condition of laminar flow along a surface (i.e., the continuum-level velocity of a fluid next to a surface is zero in laminar flow).

A leading-edge stagnation point is a combination of type "a" and type "c" impacts, which is explicit along the stagnation line. Trailing-edge stagnation point pressures are a type "b" impacts, but my include both type "b" and type "c" impacts in ground-effect flight. Pressure generation from oncoming air on a concave downward surface is similar to the progression of the leading-edge stagnation point, but without the explicit stagnation line and stagnation point.

Ultimately, the prominence of flow around airfoil bodies does not preclude that impacting flows are the cause of higher pressures, and the molecular-level differences between pressure and flow velocity allow pressure to expand against oncoming flow as is common in front and under bodies. Pressure is a form of energy often included in enthalpy (internal energy plus pressure times volume), and while changes in rotational and vibrational energies occur in molecular collisions, the billiard-ball model of Figure 11 is sufficiently accurate for this application.

The Speed of Sound and Induced Thrust – Pressure extends its influence and dissipates in a gas at the velocity gas molecules with accounting for the frequency of collisions, which is often characterized as the speed of sound. Abbott's in-depth discussion of airfoils includes a discussion of how pressure gradients propagate at the speed of sound, but this discussion is in a chapter on effects of compressibility at subsonic speeds. And so, the speed of sound is identified as important in airfoil aerodynamics, but is only mentioned in discussions of compressible flow and supersonic speeds. This is understandable since pressure is properly associated with increased gas density. Despite this impression, the pressure profiles of this paper clearly identify effect pressure dissipation when air is modelled as an incompressible fluid at lower speeds.

The numerical solution accounts for pressure gradients by a mechanism other than compression of air. Whether these accounting methods are fundamentally accurate or not, the overall trends appear to be fundamentally correct and decades of CFD applications testifies to the veracity of CFD methods in aircraft design.

Figure 12 illustrates how sources of pressure extend their impact and dissipate on a NACA-type airfoil at different angles of attack including prevalent leading-edge and trailing-edge stagnation points. At a pitch of 6°, Principle 4 suggests the resulting L/D should be 9.5 (57/6), but the CFD results provide an L/D of 50. The high L/D of the Figure 12d airfoil can be attributed to migration of the leading-edge stagnation point below the leading edge with a diverging airflow immediately above the leading edge. A lower pressure on a surface of negative surface pitch induces thrust rather than drag on that surface (in addition to lift). The induced thrust subtracts from drag in L/D and leads to higher L/D. This phenomenon is exhibited by most aircraft wings and is a critical mechanism through which aircraft are able to take off at high angles of attack while preserving reasonable L/D efficiency.

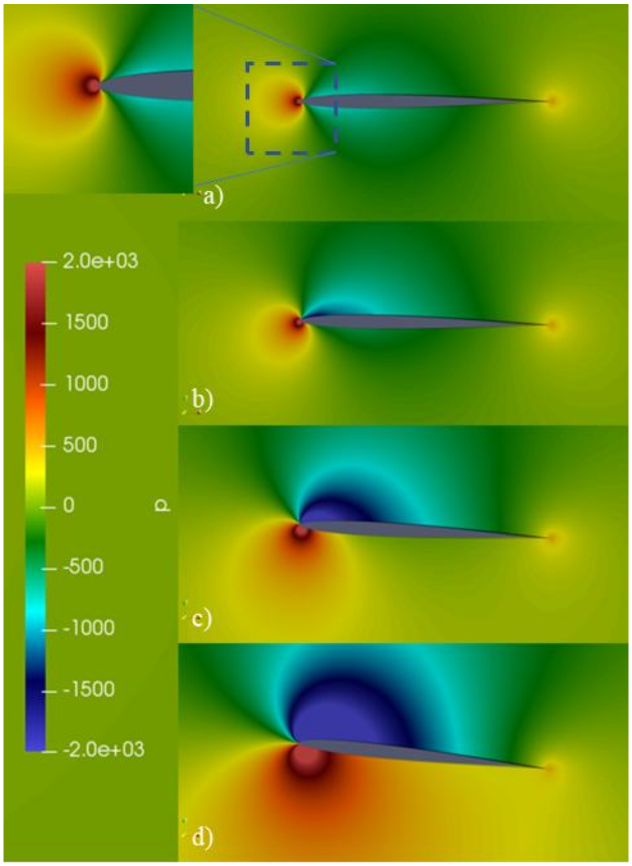

Figure 12. Pressure ($m^2/s2$) profiles of a modified NACA0006 airfoil at pitch angles relative to free stream velocity. of a) 0°, b) 1°, c) 3°, and d) 6°. Air velocity is 90 m/s with respective *L/D* of 0, 15, 37, and 50.

The manner in which induced thrust subtracts from drag in L/D is the prominent mechanism through which L/D values in excess of 50 are attained.

The primary driving force for the downward aft-ward migration of the leading-edge stagnation point is the pressure-driven flow of air from the leading-edge stagnation point to the low pressures created by diverging air flow on the upper surface. The pressure-driven flow is at the speed of sound and able to overcome oncoming air momentum until the oncoming air velocity approaches the speed of sound. As oncoming air flow approaches the speed of sound, induced thrust lessens and L/D increases. The increased drag of an aircraft as it approaches the speed of sound is often associated with the accumulation of air which cannot escape against the approaching near-sonic air. A more accurate description is that as the speed of sound is approached, induced thrust diminishes with resulting lower L/D efficiency.

Insight into New Frontiers of Aircraft Design – Principles 1-6 have provided insight into new frontiers in ground-effect flight and uses of towed-platforms to increase the capabilities of solar aircraft [3, 21, 24]. In both of these frontiers, preferred functional aircraft planforms emerge with significantly lower aspect ratios than contemporary alternatives.

Traditional explanations of the mechanism through which ground-effect enhances flight efficiency is reduced drag through the disruption of wingtip vortex formation and interrupting downwash [5, 25].

The results of this paper identify that the ground is able to increase L/D by blocking the downward dissipation of lift pressure, which in the restricted space between an aircraft and the ground, and is not accurately characterized as downwash. This work also identifies that the primary superficial impact of the ground is to increase lift (see Figure 10) rather than decrease drag. As an overall phenomenon, the ground forces more-horizontal streamlines that do not have lost work in the form of downward velocities. Extended discussions of GEFT identify that optimal GEFT aircraft have a lower cavity defined by side fences which reduce spanwise dissipation of lift forces and are effective with a low aspect ratio lifting bodies.

Advances in solar aircraft include the use of towed solar platforms of low aspect ratio. When these platforms are single-layer sheets, solar energy may be collected on the upper and lower surfaces of that lift generating sheet. The technical challenge is to generate lift on a low aspect ratio lifting body in the absence of enhancement from ground effect. The solution is the use of distributed propulsion to increase lift and decrease drag where ducted fans generate lower pressures at intakes and higher pressures at discharges. A particularly effective approach is the crossover-source where lower surface of a mid-chord ducted fan extends forward and the upper duct surface extends aft-ward. Figure 13 illustrates the crossover source including pressure profiles from 3D CFD simulations.

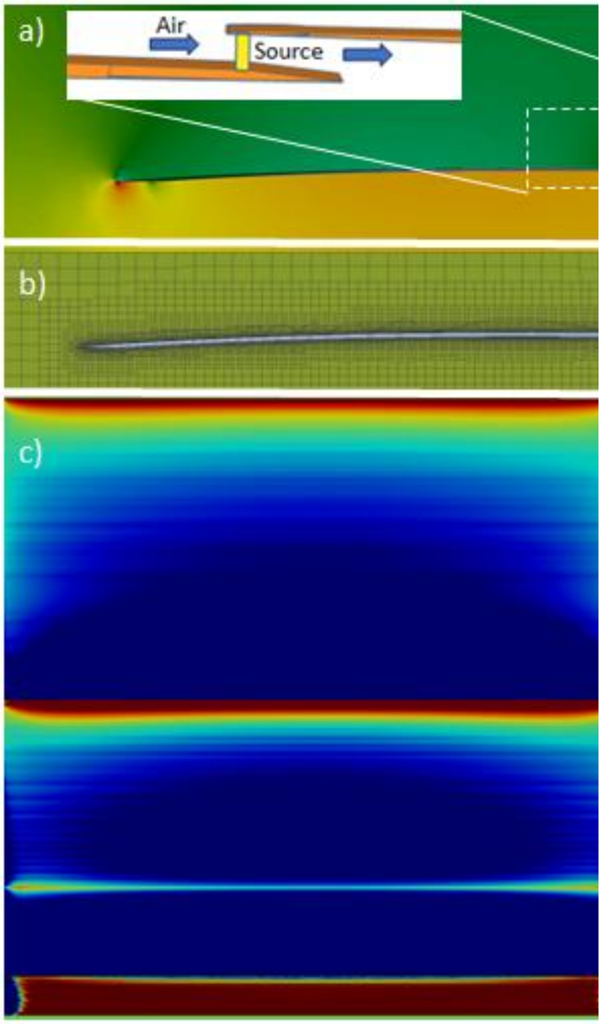

Figure 13. Pressure profile and mesh of thin cambered airfoil with mid-chord crossover Source, trailing section Lift Span, and a trailing Source. a) airfoil, b) mesh, c) top view of 3D wing, d) bottom view.

Fundamentally-Correct Interpretations - Several theories of aerodynamic lift have emerged in the past century, including:

- Bernoulli Theory of Lift
- Momentum Theory of Lift
- Turning Air Theory
- Lifting Line Theory

Most theories were developed as an analytical correlation to relate airfoil and wing properties to flight characteristics for engineering design purposes, without a priority on understanding the cause of lift pressures. All theories are correlations between pressure and other variables, and they attribute changes in pressure as a result of continuum mechanics-level changes in velocity or velocity vectors without a fundamental causality. While the correlations, and respective theories, are often accurate in correlating trends, their failures of identifying fundamental mechanisms ultimately limits their utility.

Principles 1-3 are substantiated in discrete mechanics of the molecular theory of gases where the mechanism for creating changes in pressure are a) gas flow impacting surfaces, b) collision of gas flows, and c) divergence of gas flows from a surface. Principles 1-3 are not theories, but are basic principles of physics which explain how air flow generates aerodynamic lift, and they accurately extrapolate to new applications like aerial towed platforms and GEFT.

In free flight, reversible lift is approached when lift pressures are rapidly generated over surfaces, and then rapidly relaxed before the pressure dissipates across streamlines. In ground-effect flight, the ground can block dissipation and extend lower-surface lift pressures over greater surface areas.

Distributed propulsion can be used to generate lift pressures in a constructive interference between the propulsor and the airframe. The need to attach propulsors to an airframe guarantees interference between the pressure differences created by the propulsor and the airframe. Effective application of distributed propulsion may be utilized to create constructive interference configurations rather than destructive interference configurations.

Terminology and Application – The terms downwash, vortex, and venturi effect are similar to the erroneous theories by the way they convey rather ambiguous phenomena with overall consistent trends but generally lack fundamentally accurate quantifiable trends. Significant effort has been spent to define and categorize these phenomena, but there remains a wide variety of definitions and examples in literature. [11, 12, 26-36] These terms and discussions lack causality and inclusion of pressure extension, dissipation, and blocking of dissipation which are at the core of advancing towed-platform and GEFT technologies.

The results identify that characterization of airfoil phenomena as a "venturi effect" is flawed. Whereas the term "Venturi effect" directly relates decreasing pressure with increasing velocity, while actual pressure profiles are often dominated by pressure increases or decreases as a result of flows impacting and diverging from surfaces.

Before the inflection point of a venturi restriction, air pressure increases (Principle 1) rather than decreases, as projected by the Venturi equation. At the restriction of the full venturi tube, lower pressures were achieved than projected for an ideal venturi restriction due to flow diverging from surfaces after the minimum in diameter. (Principle 2). For the Figure 7 example, a 70% reduction in pressure forward the reduction occurred due to air bypassing the duct leading to the venturi restriction.

Terms like "downwash" and "vortex" are often associated with aerodynamic lift. The more accurate interpretation of these terms are forms of lost work, where a vortex is mixing which is a fundamental form of lost work. Downwash can be an unavoidable lost work to provide rapid changes in elevation during takeoff, but in steady-level flight, the downward velocity vector component behind a lifting body will tend to dissipate as lost work (i.e., waste heat) rather than returning to free stream conditions without degradation to waste heat.

Terminology including the qualifiers Venturi, Coanda, vortex, and Bernoulli are in widespread use within the aerospace community, but not so within physics and chemical engineering; their use is often in error. For example, the "Coanda effect" is presented as a fundamental phenomenon but, while the nature of a gas to flow along a curving surface is "common," it is not a fundamental phenomenon. Chemical engineering terminology becomes more relevant in this work due to the extension of mechanisms to the molecular mechanics level. This paper presents the terms impacting, converging, diverging, expansion, and dissipation as fundamental terms and without the baggage of other terms.

Two particularly important applications emerge from this work. One application is in education due to the value of having a science consistent with molecular mechanics, continuum mechanics, and accuracy in extrapolation towards innovation, ultimately enabling global understanding of concepts that are reinforced through persistent observations. The second application is in ground-effect flight innovation with performance quantification for various digital prototypes [37-40]. 3D digital prototypes in ground-effect flight are able to reach much higher efficiency than contemporary aircraft. 3D digital prototype performance is always less than 2D airfoil performance since lateral dissipation of lift pressures is ignored in 2D airfoils. Realizing the high performance in actual vehicles is a topic of ongoing work with apriority of maximizing the information gained from digital prototypes before realization.

6. Conclusions

A century of aerospace engineering has yielded power CFD capabilities that are a mainstay of modern aircraft engineering; however, competing "schools of thought" within the industry exemplify an ongoing problem related to simple explanations that enable the human mind to understand how air flow creates aerodynamic lift. The prominent analogy of these explanations is that increased velocity leads to lower pressures; which is true but often only accounting for about half of the pressure transformations that lead to aerodynamic lift. The following six basic physics principles accurately convey how air flow is converted to aerodynamic lift and methods on how to use that lift to generate high L/D efficiency:

Principle 1. Impacting air flows create higher surface pressures.

Principle 2. Diverging air flows create lower surface pressures.

Principle 3. Air expanding from higher to lower pressures at the speed of sound extends lift pressures along streamlines, dissipates lift pressures across streamlines, and interacts with air flow to turn streamlines.

Principle 4. The L/D of a section of an airplane surface is approximately equal to 57° divided by the pitch of the surface in degrees for lower surfaces and -57° divided by the pitch for upper surfaces. The pitch angle is relative to horizontal with the nose up as positive.

Principle 5. Surfaces can be used to block loss of lift pressures leading to increased L/D. Example surfaces are winglets on wings and fences under lifting bodies.

Principle 6. For a ground-effect aircraft with a properly-designed lower fenced cavity, 3D CFD estimates of cavity lift pressures are able to approach 2D estimates, enabling 2D airfoil simulations to accurately predict actual performances in many applications.

These principles apply to steady-level flight and do not account for impact of viscosity on lift or drag.

These principles are fundamentally accurate, aligned with forces encapsulated by the Navier-Stokes equation, which enables accurate extrapolation toward innovation. Two frontiers enabled by these principles are ground-effect flight and solar towed platforms. Ground effect flight is enabled by the ground blocking the dissipation of lift forces and respective increases in L/D efficiency. Solar platform frontiers are enabled by distributed propulsion where the engine is strategically located to enhance lower pressures on upper surfaces and higher pressures on lower surfaces.

The insight gained from the studies of this paper are primarily possible due to visualization of pressure and velocity profiles that has only recently become available at relatively low costs in money and time. Another contributing factor is the serendipity of the pursuit of significant advances in solar aircraft capabilities without being stuck in decades-old paradigms of common "schools of thought" in aerospace engineering. In view of the unique circumstances of this work, it is understandable that significant flaws in the foundation of understanding how air flow creates aerodynamic lift have persisted for over half a century.

Acknowledgements

The authors would like to thank Mustansiriyah University (www.uomustansiriyah.edu.iq) Baghdad-Iraq for its support in the present work.

Conflict of interest

The authors declare no conflicts of interest regarding the current research.

Author Contribution

Galen Suppes proposed the research problem, designed experiments, and performed majority of writing.

Adam Suppes performed computational fluid dynamics and reduced simulation results to figures and tables in good format.

Harith H. Al-Moameri verified the analytical methods.

Arnold A. Lubguban verified approaches of the research problem and discussion.

References

[1] Suppes, A., and Suppes, G., "Highly-Efficient Low-AR aerial vehicles in urban transit," *Proceedings of the 2024 Transportation Research Board Annual Meeting,* January, 2024,

[2] Anonymous "Navier-Stokes Equations," [online database]https://www.comsol.com/multiphysics/navier-stokes-equations?parent=modeling-conservation-mass-energy-momentum-0402-432-302 [cited Oct 11 2024].

[3] Suppes, G., and Suppes, A., "Computational Analysis of Towed Solar Platform Aircraft," *Research Square,* 2023, pp. 1–29. https://doi.org/10.21203/rs.3.rs-4670250/v2

[4] Abbott, I.H., and Von Doenhoff, A.E., "Theory of Wing Sections: Including a Summary of Airfoil Data," Dover Publications, Inc., New York, 1949,

[5] Hurt, H.H.J., "Aerodynamics for Naval Aviators," USAF, 1965,

[6] Loyalka, S.K., and Chang, T.C., "Sound-wave propagation in a rarefied gas," *Physics of Fluids,* Vol. 22, 1979, pp. 830. 10.1080/00411457908214538

[7] Garcia, R., and Siewert, C., "The linearized Boltzmann equation: Sound-wave propagation in a rarefied gas," *Zeitschrift Fur Angewandte Mathematik Und Physik,* Vol. 57, 2005, pp. 94–122. 10.1007/s00033-005-0007-8

[8] Loyalka, S.K., "Motion of a sphere in a gas: Numerical solution of the linearized Boltzmann equation," *Physics of Fluids: Fluid Dynamics,* Vol. 4, No. 5, 1992, pp. 1049–1056. 10.1063/1.858256

[9] Loyalka, S., "On Boundary Conditions Method in the Kinetic Theory of Gases," *Zeitschrift Naturforschung Teil A,* Vol. 26, 2014, pp. 1708. 10.1515/zna-1971-1020

[10] Halloran, M., and O'Meara, S., "Wing in Ground Effect Craft Review," Aeronautical and Maritime Research Laboratory, Melbourne Victoria 3001 Australia, 1999. https://apps.dtic.mil/sti/pdfs/ADA361836.pdf

[11] Qu, Q., Wang, W., Liu, P., and Agarwal, R.K., "Airfoil Aerodynamics in Ground Effect for Wide Range of Angles of Attack," *AIAA Journal,* Vol. 53, No. 4, 2015, https://doi.org/10.2514/1.J053366

[12] Deviparameswari, K., Meenakshi, S., Akshay Kumar, N., Vigneshwaran, R., Rohini Janaki, B., Vinsiya Maria, A., Keerthana, N., Surya, B., Vetrivel, M., Thianesh, U.K., Rajarajan, S., Manikandan, P., "The Effects of Ground Clearance and Boundary Layer Blockage Factor on the Aerodynamics Performance of the Hyperloop Pod and Transonic Ground-Effect Aircraft | AIAA AVIATION Forum," *AIAA Aviation Forum,* 2021, https://doi.org/10.2514/6.2021-2586

[13] Lee, S., and Lee, J., "Optimization of Three-Dimensional Wings in Ground Effect Using Multiobjective Genetic Algorithm," *Journal of Aircraft,* Vol. 48, No. 5, 2012, https://doi.org/10.2514/1.C031328

[14] Anonymous "Lifting-line theory," 2023, https://en.wikipedia.org/w/index.php?title=Lifting-line_theory&oldid=1157579627

[15] Sears, W.R., "Some Recent Developments in Airfoil Theory," *Journal of the Aeronautical Sciences,* Vol. 23, No. 5, 1956, pp. 490–499. 10.2514/8.3588

[16] Tietjens, O.K.G., and Prandtl, L., "Fundamentals of Hydro- and Aeromechanics, Volume 1," Courier Corporation, 1939,

[17] Tietjens, O.G., "Applied hydro- and aeromechanics; based on lectures of L. Prandtl." Dover Publications, New York, 1957,

[18] NASA Glenn Research Center, and Benson, T., ""Lift from Flow Turning"," March 182004https://www.grc.nasa.gov/www/k-12/VirtualAero/BottleRocket/airplane/right2.html

[19] Anonymous "AIRFISH 8," 2023https://www.wigetworks.com/airfish-8 [cited Mar 4 2024].

[20] Blain, L., "Regent to debut its hydrofoiling ground-effect Seagliders in Hawai'i," Jan 212024https://newatlas.com/aircraft/hawaii-seaglider/ [cited Mar 8 2024].

[21] Suppes, A., and Suppes, G., "New Benchmarks in Ground-Effect Flight Energy Efficiency," July 102024https://www.researchsquare.com/article/rs-4707178/v1https://doi.org/10.21203/rs.3.rs-4707178/v1 [cited Jul 29 2024].

[22] Suppes, A., and Suppes, G., "Ground Effect Flight Transit (GEFT) – Towards Trans-Modal Sustainability," Vol. 1, 2024, https://doi.org/10.33774/coe-2024-prxvr

[23] Suppes, G., and Suppes, A., "Ground Effect Flight Transit (GEFT) – Approaches to Design," Cambridge University Press, Cambridge Open Engage, 2024. https://www.cambridge.org/engage/coe/article-details/66b2340b01103d79c5e7ab2310.33774/coe-2024-2c87q

[24] Suppes, A., and Suppes, G., "Thermodynamic Analysis of Distributed Propulsion," *Research*

Square, 2023, pp. 1–26. 10.21203/rs.3.rs-4670270/v1

[25] Anonymous "Pilot's Encyclopedia of Knowledge," Skyhorse Publishing, Inc, 2007, pp. 3–8.

[26] Qu, Q., Zuo, P., Wang, W., Liu, P., and Agarwal, R.K., "Numerical Investigation of the Aerodynamics of an Airfoil in Mutational Ground Effect," *AIAA Jouranl,* Vol. 53, 2015, https://doi.org/10.2514/1.J054155

[27] Lee, S., and Lee, J., "Aerodynamic analysis and multi-objective optimization of wings in ground effect," *Ocean Engineering,* Vol. 68, 2013, pp. 1–13. https://doi.org/10.1016/j.oceaneng.2013.04.018

[28] Hu, H., Zhang, G., Li, D., Zhang, Z., Sun, T., and Zong, Z., "Shape optimization of airfoil in ground effect based on free-form deformation utilizing sensitivity analysis and surrogate model of artificial neural network - ScienceDirect," *Ocean Engineering,* Vol. 257, 2022, pp. 111514. https://doi.org/10.1016/j.oceaneng.2022.111514

[29] Lee, J., "Computational analysis of static height stability and aerodynamics of vehicles with a fuselage, wing and tail in ground effect - ScienceDirect," *Ocean Engineering,* Vol. 168, 2018, pp. 12–22. https://doi.org/10.1016/j.oceaneng.2018.08.051

[30] Burgmann, S. Dannemann, J. & Schroder, W., "Time-resolved and volumetric PIV measurements of a transitional separation bubble on an SD7003 airfoil | SpringerLink," *Experiments in Fluids,* Vol. 44, 2007, pp. 609–622. https://doi.org/10.1007/s00348-007-0421-0

[31] Ma, Y., Zhang, W., and Elham, A., "Multidisciplinary Design Optimization of Twin-Fuselage Aircraft with Boundary-Layer-Ingesting Distributed Propulsion," *Journal of Aircraft,* Vol. 59, 2022, 10.2514/1.C036559

[32] Tse, T., and Hall, C., "Flow Field and Power Balance of a Distributed Aft-fuselage Boundary Layer Ingesting Aircraft," 2020-08-24, 10.2514/6.2020-3779

[33] Winslow, J., Otsuka, H., Govindarajan, B., and Chopra, I., "Basic Understanding of Airfoil Characteristics at Low Reynolds Numbers (104–105)," *Journal of Aircraft,* Vol. 55, 2017, pp. 1–12. 10.2514/1.C034415

[34] Klose, B., Spedding, G., and Jacobs, G., "Direct numerical simulation of cambered airfoil aerodynamics at Re = 20,000," 2021, https://doi.org/10.48550/arXiv.2108.04910

[35] Michna, J., and Rogowski, K., "Numerical Study of the Effect of the Reynolds Number and the Turbulence Intensity on the Performance of the NACA 0018 Airfoil at the Low Reynolds Number Regime," *Processes,* Vol. 10, 2022, pp. 1004. 10.3390/pr10051004

[36] Lee, D., Nonomura, T., Oyama, A., and Fujii, K., "Comparison of Numerical Methods Evaluating Airfoil Aerodynamic Characteristics at Low Reynolds Number," *Journal of Aircraft,* Vol. 52, 2015, pp. 296–306. 10.2514/1.C032721

[37] Suppes, A., Suppes, G., and Al-Moameri, H., "Overcoming Boundary-Layer Separation with Distributed Propulsion," *Sustainable Engineering and Technological Sciences,* Vol. 1, No. 01, 2025, pp. 71–89. https://doi.org/10.70516/7a9e2y30

[38] Suppes, A.B., and Suppes, G., "Thin Cambered Lifting Bodies in Ground Effect Flight," *Engrxix Engineering Archive Pre-Print,* No. 1, 2024, https://doi.org/10.31224/4136

[39] Suppes, G., and Suppes, A., "Critical Data and Thinking in Ground Effect Vehicle Design," Cambridge University Press, Cambridge Open Engage, 2024. https://www.cambridge.org/engage/https://doi.org/10.33774/coe-2024-76mzx

[40] Suppes, A., and Suppes, G., "Seamless Multimodal Passenger-Oriented Service for River and Bay Communities," *TechRxiv Preprints,* 2025, https://doi.org/10.36227/techrxiv.173932982.23714576/v1

Sustainable
Engineering and Technological Sciences
https://sets.zenithacademic.co.uk/index.php/sets/index

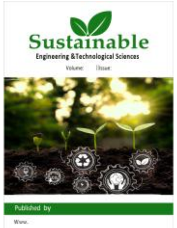

Sustainable Engineering and Technological Sciences, 01(02), 2025, pp. 32-41
DOI: https://doi.org/10.70516/n5ppe973
ISSN 3049-7787 (Print)
ISSN 3049-7795 (Online)

Evaluation of Trihalomethanes in Drinking Water of Mosul, Iraq

Zinah A. Alshrefy [1,a*]

[1] Quality Assurance and university performance department, University presidency, Northern Technical University, Mosul, Iraq

[a] Corresponding author: zena.alshrefy@ntu.edu.iq (https://orcid.org/0000-0003-0884-9570)

Article info
Received 4 February 2025
Revised 2 June 2025
Accepted 2 June 2025
Available online 1 July 2025

***Keywords**: Trihalomethanes, Water Quality, Risk Assessment, Drinking water safety*

Abstract. This study investigates the occurrence and associated health risks of trihalomethanes (THMs)—specifically bromodichloromethane (BDCM), dibromochloromethane (DBCM), and bromoform (BF)—in the domestic water supply of Mosul, Iraq. Water samples were collected from ten locations across the city between 2019 and 2020, including Al-Zuhoor, Al-Muthanna, Al-Sukar, Al-Mansour, Al-Majmoua Al-Thaqafiya, Al-Wahda, Al-Maliya, Al-Hadbaa, Al-Arabi, and Al-Tamim neighborhoods. Analysis was performed using gas chromatography with electron capture detection (GC-ECD) following USEPA Method 551.1. THM concentrations ranged from non-detectable to 69.4 µg/L, remaining below the WHO guideline of 100 µg/L. Health risk assessments were conducted using both WHO and USEPA models. Non-carcinogenic risks via ingestion pathways were found to be within acceptable limits (hazard quotient < 1), while the estimated total lifetime cancer risk from combined exposure (1.03×10^{-6}) slightly exceeded the USEPA benchmark of 1.0×10^{-6}, a threshold typically used for carcinogenic risk, indicating a marginal yet notable concern. The assessment primarily focused on oral ingestion, and further investigation into inhalation and dermal pathways, as well as impacts on sensitive subpopulations (e.g., children, elderly), is recommended. To mitigate potential health risks, improvements in water treatment—such as the implementation of advanced technologies like activated carbon filtration and better optimization of chlorination practices—are advised. The findings contribute valuable insights into water quality management and chemical exposure in urban environments of developing regions.

1. Introduction

Water disinfection using chlorine as a disinfectant is an economic and effective in water treatment for disinfection strategy and inactivation of microorganisms (Chowdhury and Champagne, 2013). Nonetheless, the hazardous organic compounds that produces as a disinfection by-product (DBP) that causes a cancer risks, as well as other acute and chronic hazards on human health.

Disinfection by chlorination, is that the medical care methodology accustomed make clean of potable, and has cause a significant decrease in mortality and morbidity from most varied diseases far-famed to be waterborne [1]. However, the potable that contain a chlorinated medical care by-products (DBP) is of concern from a public health side as a result of they will be malignant neoplastic disease [2-4]. The medical care by-product compounds that fashioned throughout medical care method is that the CHCl3, $CHBrCl_2$, $CHBr_2$, and $ClCHBr_3$, the $CHCl_3$ is assessed in cluster 2B as a probably malignant neoplastic disease to humans, supported comfortable proof of carcinogenicity in experimental animals [6-7]. CHBrCl2 may be an agent and classified as in all probability malignant neoplastic disease to humans, with comfortable proof in animals. CHBrCl2 is to be the foremost potent eutherian mammal matter. CHBr2Cl and CHBr3 area unit classified in cluster three thanks to the inconclusive genotoxicity [6-8]. The THMs risks area unit cancer and adverse copy issues like abortion, miscarriage, and feebleminded foetal development [1-3].

Chlorine chemically is a very reactive compound and also known as a strong oxidizing agent. In the 1970s, some studies cited that the chlorinated drinking water may be produces a **halogenated disinfection by-product (DBPs)**, the formation of DBPs are correlated with the concentrations of natural organic carbon (TOC) and retention time, water pH, and water temperature, so the mono-chloramine uses are increased as a secondary disinfectant in order to control the formation of DBPs in drinking water [1-2].

Trihalomethanes (THMs) compounds that formed in chlorinated water are trichloromethane (TCM, chloroform), bromodichloromethane (BDCM), dibromochloromethane (DBCM), and tribromomethane (TBM, bromoform). Brominated DBPs are formed by the competing chlorine agent during oxidation of bromide to HOBr/OBr− a brominating agent.

Halo organic compounds (THMs and HAAs) are represents the bigger mass portion of the halo-organo compounds, these organo compounds have been regulated in all states of the world. The THMs were regulated in the USA by the USEPA. The maximum permissible limit level (MPL) of 100 µg/L for total trihalomethanes (TTHM), which is the sum of the four trihalomethanes compounds. The TTHM maximum permissible limit was calculated based on water treatment and chlorination disinfection, controlling waterborne of microbial risks. The TTHMs were used as indicators to determine the treatment type and for reduce the other DBPs, and and controlling the coliforms and Escherichia coli bacterial indicators of pathogenic microorganisms [1-2, 8-10].

The chlorination of water is that the main step in treatment method for the standard of water however may well be causes a formation of undesirable organic compounds thanks to the production of DBPs throughout chlor-amination, chlorination, and ozonation method that react with a natural organic matter. The previous studies have rumored that the water chlorination could also be fashioned a probably dangerous DBPs with quite 600 DBPs detected and determined in drinking waters [9-10]. DBPs compounds square measure includes the THMs, HAAs, HALs, HKs, and element DBPs like HANs, HNMs, and HAcAms [11-15]. However, with the ne techniques in analytical procedures, rising DBPs like halobenzoquinones and iodotrihalomethanes are known [16-18].

Natural organic matter (Humic and fulvic poly organic compounds) that represent the TOC, and act as the organo precursors for the formation of hazardous organo compounds when exist with the chlorine in water treatment process, while bromide ion act as an inorganic precursor for brominated organo compounds [19-21].

Alternative disinfectants use in water treatment is also turn out unregulated DBPs that probably have a health hazard in beverage. several medicine studies have cited that health risks, related to liver, system, kidney, and central systema nervosum, magnified risk of cancer attributable to a consumption of beverage that have a DBPs and exceeds than the utmost stuff level (MCL) [5, 11–16].

Many studies have been identifying and describe the THMs formation potential and related health hazardous effects (5), where the maximum contaminant levels (MCLs) of THM was 0.080 mg/l according to USEPA (2018).

2. Methodology

2.1 Sampling

Water samples were collected from ten selected sites across the drinking water distribution network of Mosul City, covering residential and municipal zones. Sampling was conducted at different intervals over the 2019–2020 period to account for seasonal variations. Each sample was collected in 100 mL amber glass bottles containing 0.3 g of sodium thiosulfate to neutralize residual chlorine. Samples were stored at 4°C and analyzed within 24 hours to maintain integrity.

2.2 Material

All material, reagents and standards used in the present study are high quality and American Chemical Society (ACS) vendors which used in analytical laboratories.

2.3 Analytical Methods

Water samples were taken from the selected ten sites, in different periods during 2019/2020, were subjected to analysis of the trihalomethanes. Samples were collected in hundred mille Amper glass after adding 0.3 g sodium thiosulfate. The collected water samples were refrigerated at 4oC for subsequence laboratory tests.

Trihalomethanes (THMs) were extracted employing a liquid-liquid extraction with HPLC grade n-hexane, and analyses were administrated employing a gas chromatograph (GC) (7890A, Agilent, USA) with auto-sampler (7683B, Agilent, USA) equipped with Associate in Nursing lepton capture detector (ECD) supported USEPA technique 551.1 [25].

Triplicate analyses were performed among twenty-four hours once extraction for all the water samples. The calculated limit of detection (LOD) for dichlorobromomethane, dibromochloromethane, bromoform, and chloroform was ≥ zero.1 µg/L. The accuracy of the GC-ECD technique for the trihalomethanes were ninety-nine.1, 98.9, 99.3, and 99.2% for chloroform, dichlorobromomethane, dibromochloromethane, and haloform, severally.

In this study, 2 approved risk assessment models were approved by the globe Health Organization (WHO) index for additive toxicity, and also the USEPA-Approved risk assistant model. The WHO index for additive toxicity, WHO, for THMs is Associate in Nursing overall guideline price to estimate the poisonous (developmental and non-carcinogenic) risk related to chlorinated drink. The IWHO price ought to be ≤ one for compliance with WHO tips and was calculated as follows:

Where C is that the concentration of every master's degree during this study, and GV is that the WHO guideline values are established. The GV for CF is three hundred, BDCM 60, DBCM one hundred and BF one hundred, bushed µg/l [22].

The USEPA approved Risk model that interested in several researchers [5-9]. The USEPA Risk assessment model is ready to estimating the toxicologic risks (toxic and non-carcinogenic risks) and malignant neoplastic disease risks.

Toxicologic risks, expressed because the hazard quotient (HQ), were calculated supported the comparison of actual exposure to the reference dose (RfD) as follows**:**

HQ = (Total amount ingested / body weight × exposure time × RfD)

The reference doses were cypher from toxicologic studies of exposure that demonstrate a essential result. they're expressed in units of mg/kg/day, and square measure obtainable within the Integrated Risk data system info [22] info maintained by the USEPA [25].

Carcinogenic risks of exposure to THMs concentrations were calculable by victimization the USEPA technique. malignant neoplastic disease material varied from cyanogenetic compounds in this there's no lower limit for the presence of risk. So, substance risk assessment models square measure supported the premise that risk is proportional to total life dose, and therefore the exposure metric used for malignant neoplastic disease risk assessment is that the life Average Daily Dose (LADD). The LADD is often utilized in conjunction with the Cancer Slope issue (CSF) to calculate individual excess cancer risk. it's AN estimate of the daily intake of a malignant neoplastic disease agent throughout the whole lifetime of a personal. The CSF is that the gradient of the road of the dose response curve derived from laboratory toxicologic studies, and levels of every compound square measure obtainable within the USEPA IRIS databases [25]. For master's degree species, the USEPA vary of concern is for AN augmented malignant neoplastic disease risk of 1026 i.e.1:1,000,000 [25].

3. Results & Discussion:

In the present study, the disinfectant water with chlorine was collected from Mousl city districts and analysis in order to estimate the trihalomethanes risk assessment.

The purpose of the risks assessment to ensures that the domestic water supplied for consumers are safe and comply with the local standards and regulations. The probabilistic Model achieve a lot of a total characterization of data, determine the intervals and then the chance of exposure for teams of people, together with proof, which needs additional study. It includes the employment of math empirical formula for the physic-chemical processes that give a spread of values and therefore the chance distribution for the exposure.

3.1 Chloroform (CF)

The observations of CF in El Mousl ranged from 18.3 to 46.4 µg/l with average value 29.65 µg/l, as shown in Table (1) and Figure (1).

Chloroform, is that the most typical THMs compounds, the CF found in high levels in chlorinated-water, as a result of higher OM [4-5]. The levels of chloroform different with totally types of water treatment plant (WTP). Levels of chloroform in chlorinated water in WTP and distribution systems square measure more or less doubly as high throughout hot months as throughout colder months. this can be a result of the excess levels of OMs and particularly of the upper rates of formation of medical care by-products within the raw water throughout the new amount [4-5].

The chlorination of water is one of the treatment steps in order to raising the water quality and to be safe for human uses but could be form an undesirable chemical hazard material because the formation of disinfection by-products during chloramination, chlorination, and ozonation with natural organic matter.

Since in seventies, studies have concluded that using chlorine as a disinfectant causes a a human risk of DBPs [18-20].

Two classes of DBPs that regulated by US Environmental Protection Agency with maximum permissible level (MPL) of 60 and 80 μg/L for HAAs and THMs compounds, respectively. The THMs are found in treated water through the reactions of applied chlorine and chloramine with fulvic and humic matter that found naturally in water.

Many researchers conducted their work in the monitoring of chloroform and the assessment of their carcinogenic and non-carcinogenic risks connected with public water supplies [2-3].

Table 1. Chloroform in DS of Mosul City
Parameters

samples	Unit	Range	Mean	SD	Notes
1	µg/l	19.2- 44.8	29.2	96.2	
2	µg/l	18.3- 43.6	28.4	88.4	
3	µg/l	19.6- 45.6	31.1	97.8	
4	µg/l	21.2-46.4	32.2	101.2	
5	µg/l	18.4-43.1	28.6	94.1	
6	µg/l	18.6-43.8	29.6	91.4	
7	µg/l	18.8-44.1	29.4	92.5	
8	µg/l	18.4-42.9	29.1	94.1	
9	µg/l	18.6-43.1	29.5	95.4	
10	µg/l	18.7-44.6	29.4	94.6	
Average		-	29.65	-	

SD: standard deviation; CF: chloroform

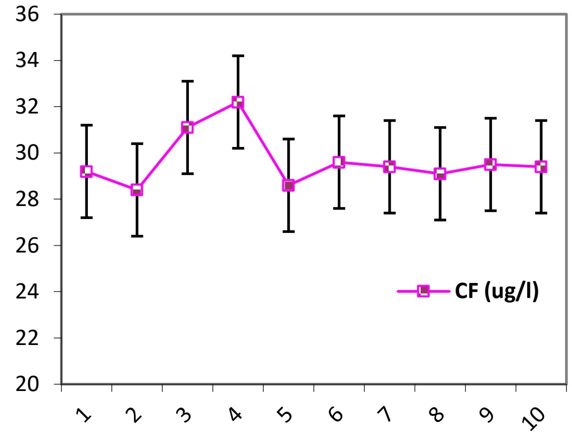

Figure 1. Average values of CF in Mosul City

3.2 Bromodichloromethane (BDCM):

The observations of BDCM in Mousl ranged from 11.3 to 28.2 µg/l with average value 17.17 µg/l, as shown in Table (2) and Figure (2).

Table 2. BDCM in DS of Mousl City

Parameters Sample	Unit	Range	Mean	SD	Notes
1	µg/l	12.5-28.2	17.4	74.2	
2		11.3-26.5	16.5	71.4	
3		12.4-25.8	17.2	77.4	
4		13.4-27.2	18.2	81.4	
5		14.2-27.8	18.6	82.4	
6		13.2-26.4	17.2	81.1	
7		13.6-26.4	17.8	84.1	
8		13.1-26.6	17.7	82.4	
9		14.3-27.5	18.1	83.6	
10		13.6-27.4	18.6	85.4	
Average		-	17.7	-	

•SD: standard deviation; DCBM: dichlorobromomethane

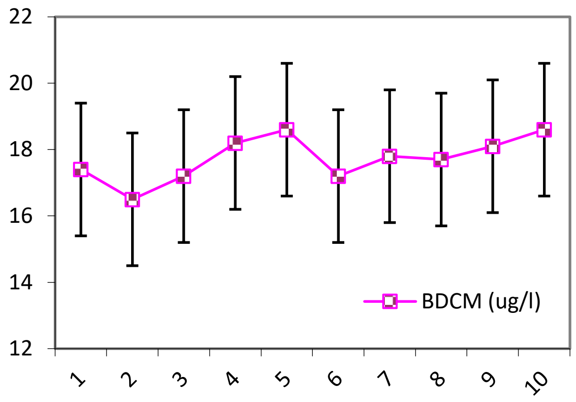

Figure 2. Average values of BDCM in Mosul City

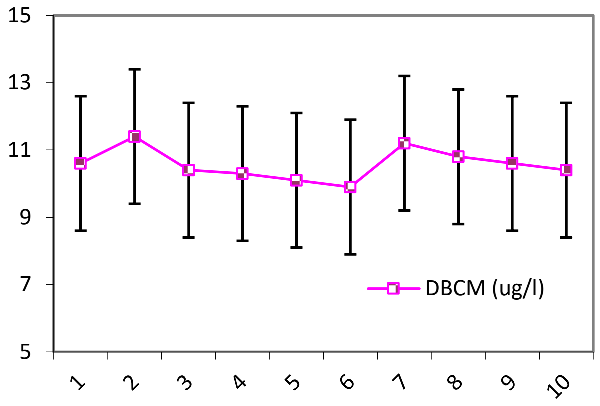

Figure 3. Average values of DBCM in El Mosul City

3.3 Dibromochloromethane (DBCM):

The observations of DBCM in El Mousl ranged from 7.2 to 14.6 µg/l with average value 10.6 µg/l, as shown in Table 3 and Figure 3.

Table 3. DBCM in DS of Mousl City

Parameters

Sample	Unit	Range	Mean	SD
1	µg/l	7.2-12.8	10.6	62.5
2	µg/l	8.2-13.1	11.4	66.2
3	µg/l	7.6-12.4	10.4	61.3
4	µg/l	7.3-12.6	10.3	58.6
5	µg/l	7.6-12.4	10.1	62.1
6	µg/l	7.3-13.8	9.9	76.2
7	µg/l	7.7-14.6	11.2	91.4
8	µg/l	7.4-13.5	10.8	75.1
9	µg/l	7.6-13.1	10.6	68.4
10	µg/l	7.2-12.8	10.4	66.2
Average		-	10.6	-

•SD: standard deviation; DBCM: dibromochloromethane.

3.4 Bromoform (BF)

The observations of BF in El Mousl ranged from ND to 3.7 µg/l with average value 1.7 µ1g/l, as shown in Table 4 and Figure 4.

Table .4. BF in DS of Mousl City

Parameters

sample	Unit	Range	Mean	SD	Notes
1	µg/l	ND-3.6	1.8	31.2	
2	µg/l	ND-4.1	2.1	36.2	
3	µg/l	ND-3.4	1.6	28.6	
4	µg/l	ND-3.4	1.7	29.6	
5	µg/l	ND-3.5	1.8	32.1	
6	µg/l	ND-3.3	1.6	29.5	
7	µg/l	ND-3.2	1.5	29.1	
8	µg/l	ND-3.4	1.7	30.5	
9	µg/l	ND-3.7	1.9	32.1	
10	µg/l	ND-3.3	1.6	29.6	
Average		-	1.7	-	

•SD: standard deviation; BF: bromoform.

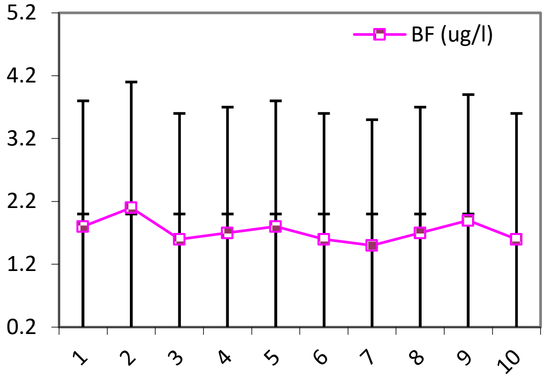

Figure 4. Average values of BF in Mousl City

Estimation of cancer risk for brominated compounds

3.5 Chloroform

The carcinogenic risk for CF is shown in Fig.5. The mean calculated value of hazard risk for amount trihalomethanes in domestic water samples was acceptable level (0.1702). The risk assessment of chloroform trichloromethane (HIi) ranged from 0.0161 to 0.0183 with average value 0.0168, as shown in Figure 5. THM could be existing in water for human public supply at high levels that may be healthy causing adverse effects for the inhabitants. Consumptions of drinking water that had THMs may be reaching to liver and kidney and causing adverse impacts for both liver and kidney, and also immune, nervous, and reproductive systems disorders [8-12]. Observation data of THMs and estimated jeopardy concluded that a correlation between the cancers of bladder, colon and rectum and these compounds in water uptake. Different countries put regularization Synonyms/Hypernyms (Ordered by Estimated Frequency) of noun value that shouldn't be to exceed those values.

Table 5. CF risk assessment

Site	C_{ai}	EF	ED	BW	AT	IR_a	RfD_i	HI_i
1	0.0292	365	70	75	25550	2	0.047	0.0166
2	0.0284	365	70	75	25550	2	0.047	0.0161
3	0.0311	365	70	75	25550	2	0.047	0.0176
4	0.0322	365	70	75	25550	2	0.047	0.0183
5	0.0286	365	70	75	25550	2	0.047	0.0162
6	0.0296	365	70	75	25550	2	0.047	0.0168
7	0.0294	365	70	75	25550	2	0.047	0.0167
8	0.0291	365	70	75	25550	2	0.047	0.0165
9	0.0295	365	70	75	25550	2	0.047	0.0167
10	0.0294	365	70	75	25550	2	0.047	0.0167
Control	0.3	365	70	75	25550	2	0.047	0.1702

HIi: non-cancer hazard quotient, EF: exposure frequency (d/y); ED: exposure duration (y); BW: body weight (kg); RfDi: reference dose for chloroform (mg/kg^{-d})

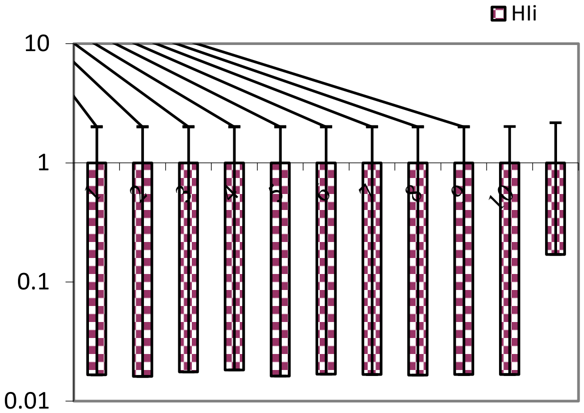

Figure 5. CF risk assessment in Mousl City

3.6 BDCM

The carcinogenic risk for BDCM is shown in Figure 6. The mean calculated value of hazard cancer risk for trihalomethanes due to treated water uptake is in the acceptable low risk (99.2×10^{-6}). The risk assessment of BDCM (HIi) ranged from 27.3×10^{-6} to 30.8×10^{-6} with average value 2.9×10^{-5} as shown in Figure 6.

Table 6. BDCM risk assessment

Site	C_{ai}	EF	ED	BW	AT	IR_a	RfD_i	HI_i
1	0.0174	365	70	75	25550	2	0.062	28.8E-6
2	0.0165	365	70	75	25550	2	0.062	27.3E-6
3	0.0172	365	70	75	25550	2	0.062	28.4E-6
4	0.0182	365	70	75	25550	2	0.062	30.1E-6
5	0.0186	365	70	75	25550	2	0.062	30.8E-6
6	0.0172	365	70	75	25550	2	0.062	28.4E-6
7	0.0178	365	70	75	25550	2	0.062	29.4E-6
8	0.0177	365	70	75	25550	2	0.062	29.3E-6
9	0.0181	365	70	75	25550	2	0.062	29.9E-6
10	0.0186	365	70	75	25550	2	0.062	30.8E-6
Control	0.06	365	70	75	25550	2	0.062	99.2E-6

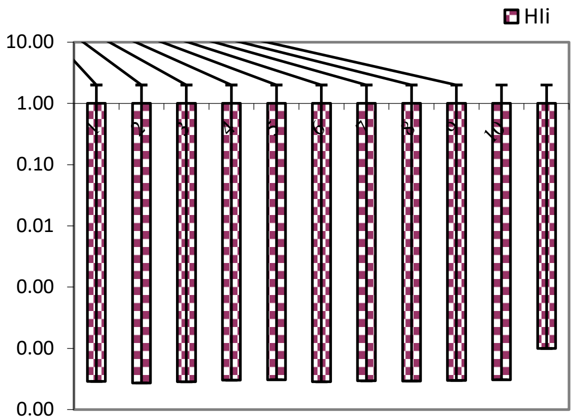

Figure 6. DCBM risk assessment in Mosul City

3.7 DBCM

The carcinogenic risk for DBCM is shown in Figure 7. The mean calculated value of hazard cancer risk for trihalomethanes due to treated water uptake is in the acceptable low risk (134.4 x 10^{-6}). The risk assessment of DBCM (HIi) ranged from 22.2 x 10^{-6} to 25.5 x 10^{-6} with average value 2.37 x 10^{-6}, as shown in Figure 7.

Table 7. DBCM risk assessment

Site	C_{ai}	EF	ED	BW	AT	IR_a	RfD_i	HI_i
1	0.0106	365	70	75	25550	2	0.084	23.7E-6
2	0.0114	365	70	75	25550	2	0.084	25.5E-6
3	0.0104	365	70	75	25550	2	0.084	23.3E-6
4	0.0103	365	70	75	25550	2	0.084	23.1E-6
5	0.0101	365	70	75	25550	2	0.084	22.6E-6
6	0.0099	365	70	75	25550	2	0.084	22.2E-6
7	0.0112	365	70	75	25550	2	0.084	25.1E-6
8	0.0108	365	70	75	25550	2	0.084	24.2E-6
9	0.0106	365	70	75	25550	2	0.084	23.7E-6
10	0.0104	365	70	75	25550	2	0.084	23.3E-6
Control	0.06	365	70	75	25550	2	0.084	134.4E-6

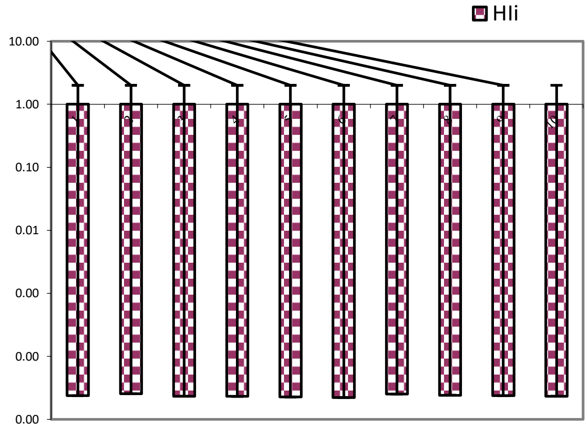

Figure 7. DBCM risk assessment in Mousl City

3.8 BF

The carcinogenic risk for BF is shown in Fig.8, the mean calculated value of hazard cancer risk for trihalomethanes due to treated water uptake is in the acceptable low risk (134.4 x $10^{\wedge -6}$). The risk assessment of BF (HIi) ranged from 3.4 x $10^{\wedge -6}$ to 4.0 x $10^{\wedge -6}$ with average value 3.66 x $10^{\wedge -6}$, as shown in Figure (8).

Table 8. BF risk assessment

Site	C_{ai}	EF	ED	BW	AT	IR_a	RfD_i	HI_i
1	0.0018	365	70	75	25550	2	0.079	3.8E-6
2	0.0021	365	70	75	25550	2	0.079	4.4E-6
3	0.0016	365	70	75	25550	2	0.079	3.4E-6
4	0.0017	365	70	75	25550	2	0.079	3.6E-6
5	0.0018	365	70	75	25550	2	0.079	3.8E-6
6	0.0016	365	70	75	25550	2	0.079	3.4E-6
z 7	0.0015	365	70	75	25550	2	0.079	3.2E-6
8	0.0017	365	70	75	25550	2	0.079	3.6E-6
9	0.0019	365	70	75	25550	2	0.079	4.0E-6
10	0.0016	365	70	75	25550	2	0.079	3.4E-6
Control	0.06	365	70	75	25550	2	0.084	134.4E-6

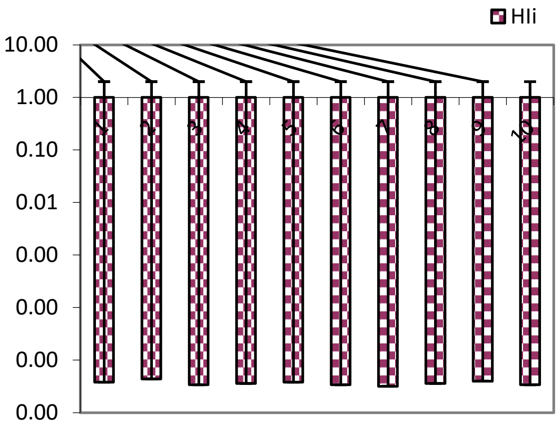

Figure 8. BF risk assessment in Mousl City

3.9 THMs

The carcinogenic risk for THMs is shown in Figure 9. The mean calculated value of hazard cancer risk for trihalomethanes due to treated water uptake is in the acceptable low risk (165.3 x 10^{-6}). The risk assessment of THMs (HIi) ranged from 96.4 x 10^{-6} to 103.2 x 10^{-6} with average value 9.87 x 10^{-6}, as shown in Figure 9.

Table 9. THMs risk assessment

Site	C_{ai}	EF	ED	BW	AT	IR_a	RfD_i	HI_i
1	0.059	365	70	75	25550	2	0.062	97.5E-6
2	0.0584	365	70	75	25550	2	0.062	96.6E-6
3	0.0603	365	70	75	25550	2	0.062	99.7E-6
4	0.0624	365	70	75	25550	2	0.062	103.2E-6
5	0.0591	365	70	75	25550	2	0.062	97.7E-6
6	0.0583	365	70	75	25550	2	0.062	96.4E-6
7	0.0599	365	70	75	25550	2	0.062	99.0E-6
8	0.0593	365	70	75	25550	2	0.062	98.0E-6
9	0.0601	365	70	75	25550	2	0.062	99.4E-6
10	0.06	365	70	75	25550	2	0.062	99.2E-6
Control	0.1	365	70	75	25550	2	0.062	165.3E-6

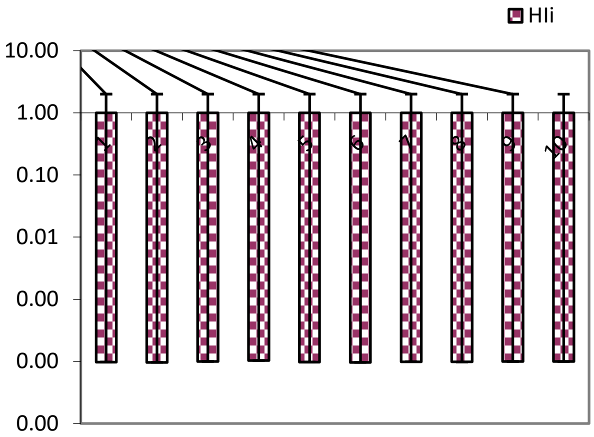

Figure 9. THMs risk assessment in Mousl City

From the observation of THMs and its compounds, the calculation of IWHO risk index was 0.45 and less than 1.0, thus ensures that the drinking water in Mousl was safe and have low risks according to WHO index.

BDCM > DBCM > bromoform > chloroform. This observation was complying with the WHO guidelines and THMs (Stalter et al. 2016). The minimum level of chloroform risk was less than 10−6 (negligible risk), that could be because of the presence of brominated THMs compounds over-chlorinated ones in water samples. While, with another researches, chloroform have the lower

4. Conclusions

The present study summarized the following points of conclusions;

•The values of THMs and its species are complying with the WHO and USEPA standards.

•The observation of THMs showed that, the values of CF is the highest value, and BF is the lowest value and nearly not detected.

•The parameters that cause high formation of THMs should be reduced by coagulation-flocculation, AC, and RO technology.

•To control the health hazard of THMs, so the break point chlorination dose of chlorine should be applied, and the THMs, should be investigated and recorded in water networks.

•The USEPA toxicity of THMs concentrations of CF, BDCM, DBCM and BF in the water networks are not exceeded than WHO guideline values for the investigated sites, and so it's have low adverse toxic and non-carcinogenic risks in health impacts, but THMs concentrations are within the WHO guidelines.

•The lifetime cancer risk for the THMs components via multi pathway exposure routes are $1.03\times10^{\wedge-6}$which was slightly higher than the $1.0\times10^{\wedge-6}$ that recommended by the USEPA.

Acknowledgements

The author acknowledges the lab staff of the Northern Technical University for their assist in conducting this research.

Conflict of interest

The authors declare no conflicts of interest regarding the current research.

Author Contribution

For example:

Z.A. Alshrefy: proposed the research problem, developed the theory, verified the analytical methods, and discussed the results and writing the paper.

References

[1] S. Chowdhury, (2013) "Exposure assessment for trihalomethanes in municipal drinking water and risk reduction strategy," Science of the Total Environment, vol. 463-464, pp. 922–930, 2013.

[2] P. Ioannou, P. Charisiadis, S. S. Andra, and K. C. Makris, (2016) "Occurrence and variability of iodinated trihalomethanes concentrations within two drinking-water distribution networks," Science ofThe Total Environment. Part A, pp. 505–513, 2016.

[3] W. B. Y. Jianrong,W.Wuyi, Y. Linsheng, T. Jing, and H. Zhijiu, (2010) "Spatial and temporal evaluations of disnfection by-products in drinking water distribution system in Beijing, China," Science of the Total Environment, vol. 408, pp. 4600–4606, 2010.

[4] T. Karanfil, S.W. Krasner, P.Westerhoff, andY.F.Xie, "Disinfection by-products in drinking water: Information, occurrence, health effects and control," American Chemical Society, vol. Washington, DC, USA, pp. 2–19, 2008.

[5] S. Pan,W. An, H. Li,M. Su, J. Zhang, and M. Yang, (2014) "Cancer risk assessment on trihalomethanes and haloacetic acids in drinking water of China using disability-adjusted life years," Journal of Hazardous Materials, vol. 280, pp. 288–294, 2014.

[6] E. Righi, P. Bechtold,D. Tortorici et al., (2012) "Trihalomethanes, chlorite, chlorate indrinkingwater and risk of congenital anomalies: a population-based case-control study in Northern Italy," Environmental Research, vol. 116, pp. 66–73, 2012.

[7] D. Stalter, E. O'Malley, U. von Gunten, and B. I. Escher, (2016) "Fingerprinting the reactive toxicity pathways of 50 drinking water disinfection by-products," Water Research, vol. 91, 2016.

[8] Y. Komaki, B. J.Mari˜nas, and M. J. Plewa, (2014) "Toxicity of drinking water disinfection byproducts: Cell cycle alterations induced by themonohaloacetonitriles," Environmental Science and Technology, vol. 48, no. 19, pp. 11662–11669, 2014.

[9] M. J. Plewa, J. E. Simmons, S. D. Richardson, and E. D. Wagner, (2010) "Mammalian cell cytotoxicity and genotoxicity of the haloacetic acids, a major class of drinking water disinfection by-products," Environmental and Molecular Mutagenesis, vol. 51, no. 8-9, pp. 871–878, 2010.

[10] M.B.Rahman, T. Driscoll,C.Cowie, andB. K. Armtrong, (2017) "Disinfection by-products in drinking water and colorectal cancer: a meta-analysis," International Journal of Epidemiology, vol. 39, no. 3, pp. 733–745.

[11] R. Sayess, A. Khalil, M. Shah, D. A. Reckhow, and K. J. Godri Pollitt, (2017) "Comparative cytotoxicity of six iodinated disinfection byproducts on nontransformed epithelial human colon cells," Environmental Science & Technology Letters, vol. 4, no. 4, pp. 143–148, 2017.

[12] S. D. Richardson, M. J. Plewa, E. D. Wagner, R. Schweny, and D. M.Demarini, (2007) "Occurrence, genotoxicity and carcinogenicity of regulated and emerging disinfection by-products in drinking water: a review and roadmap for research," Mutation Research/ Reviews inMutation Research, vol. 636, pp. 178–242, 2007.

[13] M. J. Plewa, M. G. Muellner, S. D. Richardson et al., (2008) "Occurrence, synthesis, and mammalian cell cytotoxicity and genotoxicity of haloacetamides: An

emerging class of nitrogenous drinking water disinfection byproducts,” Environmental Science & Technology, vol. 42, no. 3, pp. 955–961, 2008.

[14] S. R. Bielmeier, A. S. Murr, D. S. Best et al., (2007) “Effects of bromodichloromethane on ex vivo and in vitro luteal function and bromodichloromethane tissue dosimetry in the pregnant F344 rat,” Toxicology in Vitro, vol. 21, no. 5, pp. 919–928, 2007.

[15] S.W. Krasner, (2009) “The formation and control of emerging disinfection by-products of health concern,” Philosophical Transactions of the Royal Society A: Mathematical, Physical and Engineering Sciences, vol. 367, no. 1904, pp. 4077–4095, 2009.

[16] S. W. Krasner, M. S. Dale, C. F. T. Lee, E. A. Garcia,W. Mitch, and U. Von Gunten, (2010) “Effect of water quality and operational parameters on DBP formation during chloramination: NDMA versus halogenated DBPs,” in Proceedings of the Annual Conference, AmericanWaterWorks Association, p. 46, 2010.

[17] L. Liang and P. C. Singer, (2003) “Factors influencing the formation and relative distribution of haloacetic acids and trihalomethanes in drinking water,” Environmental Science & Technology, vol. 37, no. 13, pp. 2920–2928, 2003.

[18] E. M. R. Souaya, A. M. Abdullah, and M. Mossad, (2015) “Factors affecting on formation of DBPs in greater Cairo drinking water,” Organic Chemistry: Current Research, vol. 4, no. 5, p. 2, 2015.

[19] B. Ye, W. Wang, L. Yang, and J. Wei, (2011) “Formation and modeling of disinfection by-products in drinking water of six cities in China,” Journal of Environmental Monitoring, vol. 13, no. 5, pp. 1271–1275, 2011.

[20] S. E.Hrudey and J.W. A. Charrois, (2012)Disinfection By-products and Human Health, IWA Publishing, London, UK, 2012.

[21] T. Bond, J. Huang, M. R. Templeton, and N. Graham, (2011) “Occurrence and control of nitrogenous disinfection by-products in drinking water - a review,” Water Research, vol. 45, pp. 4341– 4354, 2011.

[22] RAIS (2005). Risk Assessment Information System. Accessed at http://rais.ornl.gov/homepage/rap_docs.shtml, 3 December, 2009.

[23] WHO (2005). Trihalomethanes in drinking water: Background document for development of WHO guidelines for drinking water quality.WHO/SDE/WSH/05.08/64.

[24] IRIS (2005). Integrated Risk Information System. Cincinnati, Ohio: United States Environmental Protection Agency. Accessed at http://www.epa.gov/iris, December, 2009.

[25] USEPA., Controlling Disinfection By-Products and Microbial Contaminants in Drinking Water, EPA: 600-R-01-110, United States Environmental Protection Agency, 2013.